Remote Sensing of Environment 303 (2024) 113986

Contents lists available at ScienceDirect

Remote Sensing of Environment

journal homepage: www.elsevier.com/locate/rse

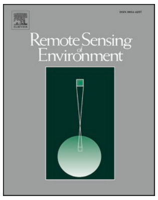

On-orbit calibration and performance of the EMIT imaging spectrometer

David R. Thompson[a,*], Robert O. Green[a], Christine Bradley[a], Philip G. Brodrick[a], Natalie Mahowald[o], Eyal Ben Dor[b], Matthew Bennett[a], Michael Bernas[a], Nimrod Carmon[a], K. Dana Chadwick[a], Roger N. Clark[c], Red Willow Coleman[a], Evan Cox[k], Ernesto Diaz[a], Michael L. Eastwood[a], Regina Eckert[a], Bethany L. Ehlmann[d], Paul Ginoux[e], María Gonçalves Ageitos[f,j], Kathleen Grant[h], Luis Guanter[i], Daniela Heller Pearlshtien[b], Mark Helmlinger[a], Harrison Herzog[a], Todd Hoefen[k], Yue Huang[l,m], Abigail Keebler[d], Olga Kalashnikova[a], Didier Keymeulen[a], Raymond Kokaly[k], Martina Klose[l], Longlei Li[o], Sarah R. Lundeen[a], John Meyer[k], Elizabeth Middleton[p], Ron L. Miller[m,n], Pantazis Mouroulis[a], Bogdan Oaida[a], Vincenzo Obiso[f,m], Francisco Ochoa[q], Winston Olson-Duvall[a], Gregory S. Okin[q], Thomas H. Painter[q,r], Carlos Pérez García-Pando[f,g], Randy Pollock[s], Vincent Realmuto[a], Lucas Shaw[a], Peter Sullivan[a], Gregg Swayze[k], Erik Thingvold[a], Andrew K. Thorpe[a], Suresh Vannan[a], Catalina Villarreal[a], Charlene Ung[a], Daniel W. Wilson[a], Sander Zandbergen[a]

[a] *Jet Propulsion Laboratory, California Institute of Technology, Pasadena, CA, USA*
[b] *Tel Aviv University, Tel Aviv, Israel*
[c] *Planetary Science Institute, Tucson, AZ, USA*
[d] *California Institute of Technology, Pasadena, CA, USA*
[e] *NOAA Geophysical Fluid Dynamics Laboratory, Princeton, NJ, USA*
[f] *Barcelona Supercomputing Center, Barcelona, Spain.*
[g] *Catalan Institution for Research and Advanced Studies, ICREA, Barcelona, Spain*
[h] *University of Southern California, Los Angeles, CA, USA*
[i] *Universitat Politècnica de València, Valencia, Spain*
[j] *Universitat Politècnica de Catalunya, Barcelona, Spain*
[k] *United States Geological Survey, Denver, CO, USA*
[l] *Karlsruhe Institute of Technology, Karlsruhe, Germany*
[m] *NASA Goddard Institute for Space Studies, New York, NY, USA*
[n] *Columbia University, New York, NY, USA*
[o] *Cornell University, Ithaca, NY, USA*
[p] *NASA Goddard Space Flight Center, Greenbelt, MD, USA.*
[q] *University of California Los Angeles, Los Angeles, CA, USA*
[r] *Airborne Snow Observatories, Inc., Mammoth Lakes, CA, USA*
[s] *Victoria University of Wellington, Wellington, New Zealand*

ARTICLE INFO

Keywords:
Imaging spectroscopy
Hyperspectral imagery
Mineral dust cycle
Radiative forcing
EMIT
NASA
International space station
Remote sensing
Mineralogy

ABSTRACT

The Earth surface Mineral dust source InvesTigation (EMIT) is a remote visible to shortwave infrared (VSWIR) imaging spectrometer that has been operating onboard the International Space Station since July 2022. This article describes EMIT's on-orbit spectroradiometric calibration and validation. Accurate spectroscopy is vital to achieve consistent mapping results with orbital imaging spectrometers. EMIT takes a unique approach to this challenge, with just six optical elements, no shutter, and no onboard calibration systems. Its simple design focuses on uniformity and stability to enable vicarious spectroradiometric calibration. Our experiments demonstrate that this approach is successful, approaching the fidelity of manual field spectroscopy in some cases, and enabling new and more accurate products across diverse Earth science disciplines. EMIT achieves several notable firsts for an instrument of its class. It demonstrates successful on-orbit adjustments of Focal Plane Array (FPA)

---

* Corresponding author.
E-mail address: david.r.thompson@jpl.nasa.gov (D.R. Thompson).

https://doi.org/10.1016/j.rse.2023.113986
Received 17 September 2023; Received in revised form 20 November 2023; Accepted 27 December 2023

Calibration
Validation
Atmospheric correction
Visible-shortwave infrared spectroscopy

alignment with sub-micron precision. It offers spectral uniformity better than 98%. Optical artifacts in the measurement channels are at least three orders of magnitude below the primary solar-reflected surface signals. Its noise performance enables percent-level discrimination in the depths of mineral absorption features. In these aspects, EMIT satisfies the stringent performance needs for the next generation of VSWIR imaging spectrometers to observe the Earth's ecosystems, geology, and water resources.

1. Introduction

The Visible to Shortwave Infrared (VSWIR) spectral range is sensitive to diverse Earth surface properties, making it useful for a wide range of remote sensing applications. Imaging spectrometers, also known as hyperspectral imagers, acquire rasters of spectra to map geophysical phenomena. They have been used to study terrestrial and aquatic ecosystems, mineral and water resources, greenhouse gas point sources, and more. The first imaging spectrometers were developed over 40 years ago (Goetz and Srivastava, 1985), but they have recently reached a new stage of maturity with orbital instruments conducting global investigations. These missions include the DLR Earth Sensing Imaging Spectrometer, DESIS (Alonso et al., 2019), the PRecursore IperSpettrale della Missione Applicativa, PRISMA (Cogliati et al., 2021), the Hyperspectral Imager Suite, HISUI (Matsunaga et al., 2020), and the Environmental Mapping and Analysis Program, EnMAP (Guanter et al., 2015; Chabrillat et al., 2020). Upcoming missions like the Copernicus Hyperspectral Imaging Mission for the Environment (CHIME; Nieke and Rast, 2018), and the Surface Biology and Geology (SBG) investigation (Cawse-Nicholson et al., 2021) will provide regular coverage of Earth's entire land area and coastal waters. Simultaneously, advances in computing enable more sophisticated algorithms, portending a new era of spectroscopic remote sensing.

State of the art spectroscopic analyses require accurate calibration. While the Earth's surface reflectance is spectrally smooth, atmospheric absorption features are sharp. This makes geophysical retrievals sensitive to wavelength miscalibrations at the sub-nanometer level. Atmospheric errors often exceed instrument noise as a source of measurement uncertainty, and can introduce atmosphere-dependent errors leading to regional biases in global maps (Carmon et al., 2020). Precise knowledge of spectral response functions is critical to preserve atmospheric absorption shapes. Moreover, high radiometric accuracy is needed to remove atmospheric distortions by Rayleigh scattering. High uniformity of both radiometric and spectral calibration is needed for consistent surface property measurements throughout the instrument field of view. In these and other ways, the performance of remote spectroscopy is often limited by calibration uncertainty rather than instrument noise. Improving spectroradiometric accuracy will be critical to fulfill the promise of future missions.

This paper describes the on-orbit calibration and validation of the Earth surface Mineral dust source InvesTigation (EMIT), a high performance VSWIR imaging spectrometer. EMIT was sponsored by the National Aeronautics and Space Administration (NASA) and developed at the Jet Propulsion Laboratory (Green et al., 2020). It is now installed on the International Space Station (ISS, Fig. 1), where it is mapping the mineralogy of Earth's mineral dust forming regions. These measurements will constrain the composition of the emitted dust, enabling Earth System Models to predict the capacity of these particles to absorb solar radiation, along with the associated radiative forcing and climate response (Connelly et al., 2021). The EMIT Instrument launched to the ISS on July 14, 2022 and was installed on the port side of the truss structure in the ExPReSS Logistics Carrier-1 (ELC1) rack (Cook, 2004). It measured first light on July 28, successfully completed on-orbit comissioning, and began science operations. At the time of this writing, EMIT has acquired over 60,000 scenes globally, with more arriving every day.

EMIT is a remote imaging spectrometer based on the Dyson pushbroom design (Bradley et al., 2020). It measures the 380–2500 nm range using a single cryogenic Focal Plane Array (FPA) with a channel spacing of approximately 7.5 nm. This range captures minerals' electronic absorptions in the visible range and vibrational overtones in the shortwave infrared. EMIT's swath spans a 74 km with approximately 60 m ground sampling to measure mineralogy in fallow farm fields. Its radiometric precision is sufficient to detect a 2% change in the hematite absorption feature, a difference which, if it appeared throughout North Africa, could change the net contribution of global dust-related atmospheric forcing from heating to cooling or vice versa. EMIT also carries a flight electronics suite: the Focal Plane Interface Electronics-Analog (FPIE-A), which digitizes signals from the FPA; and the Focal Plane Interface Electronics-Digital (FPIE-D), a high performance embedded computing system (Keymeulen et al., 2022) that processes the data and applies onboard cloud screening and compression to reduce data volumes. Unlike contemporary instruments of its class, EMIT carries no onboard shutter or calibration mechanism. Its simple design emphasizes spectral fidelity and radiometric stability to enable on-orbit calibration with vicarious targets.

This manuscript reports EMIT's post-launch calibration and performance. It documents our methods and quantifies data product accuracy. We focus on spectral and radiometric characteristics since these are central to EMIT's science objectives. Section 2 presents spectral calibration, which describes the sensitivity of each Focal Plane Array (FPA) element to different wavelengths. We discuss channel center wavelengths, spectral response functions, and corrections for stray spectral response. Section 3 describes radiometric calibration, which translates instrument digital numbers to units of radiance. We describe corrections for optical ghosts, measurement and validation of radiometric calibration coefficients, measurement of spatial nonuniformities, and corrections for inoperable FPA elements. We evaluate radiometric performance over several field sites where ground truth reflectance data are available. Then, we compare EMIT's instrument noise to radiometric models constructed in the laboratory. Section 4 concludes with the implications for EMIT science and future missions. EMIT shows the spectral and radiometric accuracy now achievable by contemporary instruments, demonstrating the performance required for future missions like ESA's CHIME and NASA's SBG. These data are already enabling groundbreaking new science, such as continental scale mineral maps of

Fig. 1. EMIT deployed to the ISS. EMIT is the white box mounted at the lower left on the ELC1 rack at the top of the image. Credit: NASA.

unprecedented detail (Brodrick et al., 2023), and the detection of hundreds of methane superemitter facilities to support global greenhouse gas mitigation (Thorpe et al., 2023).

For reproducibility, all code and data for these experiments are available from public archives. The radiometric calibration code and files are available from the public EMIT mission repository (Olson-Duvall et al., 2022). EMIT mission data is available at the NASA's Land Processes Distributed Active Archive Center (LP DAAC) (Green et al., 2022). EMIT also produces a range of derived data products, including surface reflectance, mineral maps, and Earth system model runs. We focus here on the initial calibration, but still use atmospheric radiative transfer models in several experiments. Code to configure and run these models is available from the ISOFIT repository (Thompson et al., 2019b). In situ field data is available from the United States Geological Survey (USGS) (Meyer et al.,2023a, 2023b).

2. Spectral calibration

Imaging spectrometers view the Earth through a range of sharp atmospheric absorption features. Analysts model these absorptions to estimate the surface reflectance signal. Fig. 2 shows the example of a vegetated pixel from EMIT scene emit20220820t035232. The EMIT scene IDs indicate the Coordinated Universal Time (UTC) timestamp of the acquisition; for example, emit20220820t035232 was acquired on August 20, 2022 at 03:52:32 UTC. Additional metadata for any particular scene is available from the NASA distributed archive (Green et al., 2022). The right panel of Fig. 2 shows the simulated radiance at fine spectral sampling and the actual measurement at coarser spectral sampling. The instrument spectral resolution is coarser than the atmospheric features, so the center wavelength and spectral response of each channel must be known with high accuracy. Spectral uniformity at all spatial positions is highly desirable because any nonuniformities, e.g., spectral smile or tilt, impact the accuracy of atmospheric correction and the resulting reflectance (Thompson et al., 2021). The following subsections describe our procedure for measuring wavelength center calibrations and spectral response functions, and for quantifying EMIT uniformity.

2.1. Channel center wavelength calibration

The EMIT channel spacing, also known as the *dispersion*, varies with wavelength and must be determined from instrument data. We measure dispersion in the laboratory by feeding an integrating sphere with five lasers of known wavelengths. A scan mirror in the EMIT vacuum chamber translates this stimulus across the EMIT field of view. We use the laser stimulus to fit a *dispersion curve* representing channel spacing as a function of wavelength. We first initialize the dispersion curve with EMIT optical models (Bradley et al., 2020). We then fit an additive offset and multiplicative stretch to the dispersion function, finding the values which best predict the observed laser lines using a least squares approach.

The laboratory data are limited by the number and wavelength stability of the lasers, so we revise this calibration after launch using features of the Earth's atmosphere. Previous studies have measured spectral calibrations using absorption features of atmospheric gases like water vapor and oxygen (Guanter et al., 2007). Here we fit modeled atmospheric features across the entire measured range from 380 to 2500 nm, excluding the deep water vapor absorptions at 1380 nm and 1880 nm. Fitting this wide range requires estimating other parameters of the Earth's atmosphere and surface. For example, the underlying surface reflectance varies as a function of wavelength, with overlapping features that could shift the apparent positions of atmospheric absorptions. Moreover, atmospheric water vapor concentration varies spatially and temporally. These free parameters must be optimized together with the instrument calibration.

Here we use the approach of Thompson et al. (2018b) to obtain a simultaneous *maximum* a posteriori estimate of surface, atmosphere, and instrument parameters. We fit a state vector $\mathbf{x}$ which includes: the surface reflectance in each instrument channel; the atmospheric water vapor concentration in g cm^{-2}; the change in wavelength position versus the original calibration; and the change in the Full Width at Half Maximum (FWHM) of the spectral response functions. We represent the wavelength shift as a function of channel number with a four-knot cubic spline. We place knots at the extrema and at channels 520 and 1790 nm, where our optical models imply inflections in the second derivative of wavelength dispersion. The resulting spline accurately fits the predicted dispersion curve. Since the physical instrument should follow this prediction, we use the same parameterization for our on-orbit adjustments. The instrument spectral response is a single parameter representing a spectrally-uniform growth or contraction of the FWHMs relative to the laboratory estimates.

We relate the state vector $\mathbf{x}$ to the radiance measurement $\mathbf{y}$ using a forward model $\mathbf{F}(\mathbf{x})$ and random noise ε:

$$\mathbf{y} = \mathbf{F}(\mathbf{x}) + \varepsilon \tag{1}$$

The forward model gives the radiance measurement for any hemispherical directional surface reflectance spectrum $\boldsymbol{\rho}_\mathrm{s}$ using the following expression (Vermote et al., 1997):

$$\mathbf{L}_{obs} = \mathbf{F}(\mathbf{x}) = \mathbf{L}_\mathbf{a} + \frac{\mathbf{L}_\downarrow}{\mathbf{1} - \mathbf{s}\circ\boldsymbol{\rho}_\mathbf{b}}\circ\left[\mathbf{t}^{\uparrow}_{\mathbf{dir}}\circ\boldsymbol{\rho}_\mathbf{s} + \mathbf{t}^{\uparrow}_{\mathbf{dif}}\circ\boldsymbol{\rho}_\mathbf{b}\right] \tag{2}$$

where $\circ$ is element-wise multiplication and the vinculum is element-wise division. Here $\mathbf{L}_{obs}$ is the radiance at aperture. The symbol $\boldsymbol{\rho}_\mathrm{b}$ represents

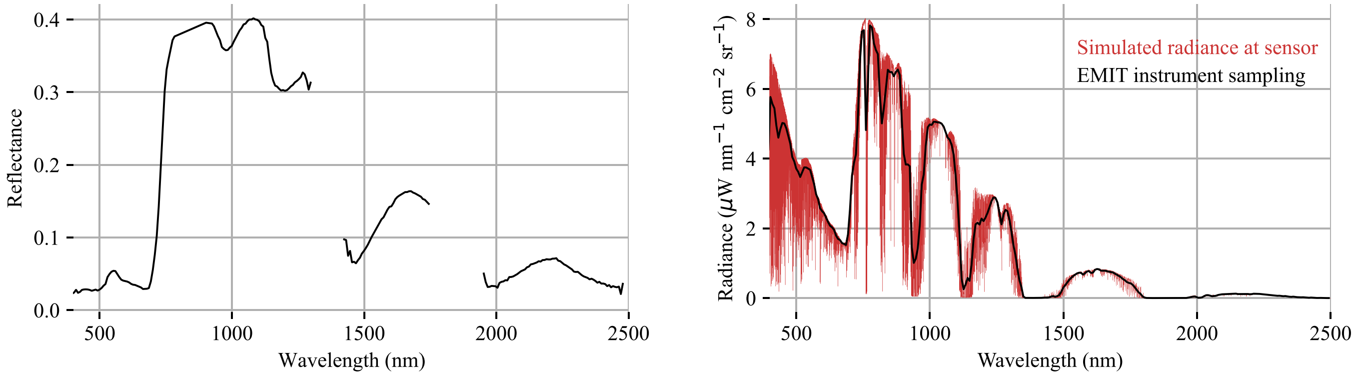

Fig. 2. Accurate estimation of surface reflectance requires accurate spectral calibration. The left panel shows an EMIT measured reflectance spectrum (scene ID emit20220820t035232). The right panel shows its simulated radiance spectrum at high resolution (red) and EMIT instrument sampling (black). Removing atmospheric effects requires modeling the instrument's sampling of these sharp atmospheric features. (For interpretation of the references to colour in this figure legend, the reader is referred to the web version of this article.)

the average reflectance of the terrain outside the pixel. For the large playa surfaces in later experiments we assume $\boldsymbol{\rho}_s$ and $\boldsymbol{\rho}_b$ are equal. The other terms are optical coefficients calculated using the MODerate resolution atmospheric TRANsmission (MODTRAN) radiative transfer model version 6.0 (Berk et al., 2014). We configure MODTRAN using the observing geometry, solar geometry, and atmospheric state, producing the upward direct beam transmittance $\mathbf{t}^{\uparrow}_{\mathbf{dir}}$, the upward diffuse transmittance $\mathbf{t}^{\uparrow}_{\mathbf{dif}}$, the spherical sky albedo at the bottom of the atmosphere $\mathbf{s}$, the path radiance $\mathbf{L_a}$, and the downwelling radiance $\mathbf{L}_{\downarrow}$ from a target with reflectance unity at the bottom of the atmosphere. We use the Fontenla et al. (2011) model for solar irradiance to calculate $\mathbf{L_a}$ and $\mathbf{L}_{\downarrow}$. We run the radiative transfer model over a grid of atmospheric state values, filling a multidimensional lookup table that can be interpolated at runtime to find the atmospheric optical coefficients for any state vector $\mathbf{x}$.

The best estimate of $\mathbf{x}$ is the one with the highest a posteriori probability, considering the measurement and any prior knowledge about probable state vector configurations. We find the most probable $\mathbf{x}$ by minimizing the following cost function (Thompson et al., 2018b):

$$\chi(\mathbf{x}) = (\mathbf{F}(\mathbf{x}) - \mathbf{y})^{\mathbf{T}}\mathbf{S}_{\varepsilon}^{-1}(\mathbf{F}(\mathbf{x}) - \mathbf{y}) + (\mathbf{x} - \mathbf{x_a})^{\mathbf{T}}\mathbf{S_a}^{-1}(\mathbf{x} - \mathbf{x_a}) \tag{3}$$

The symbol $\mathbf{S}_{\varepsilon}$ is the covariance of the zero mean observation noise ε. This term penalizes departure of the modeled radiance from the measurement, accounting for the observation noise covariance. For typical instrument performance with signal to noise ratios (SNRs) in the hundreds, the solution is insensitive to noise magnitude. Consequently, for these tests we used a diagonal noise covariance matrix with a conservative SNR of 200. We construct a more accurate noise model in Section 3.6.

The second term of eq. 3 penalizes departure of the state vector from the prior distribution. Here the prior is a multivariate Gaussian with mean $\mathbf{x_a}$ and covariance $\mathbf{S_a}$. The atmospheric elements are independent from each other and from the surface reflectance. The surface reflectance elements are correlated via a block diagonal covariance matrix describing the statistics of physical surface reflectance spectra. We select this prior from a set of multivariate Gaussian distributions as in Thompson et al. (2018b). We constructthese distributions with the sample statistics of the USGS Spectral library (Kokaly et al., 2017), and other community libraries (Herold et al., 2004; Dennison and Gardner, 2000; Thompson et al., 2019a), all of which have been manually cleaned of artifacts, curated and uploaded as EMIT mission libraries to the Ecological Spectral Information System (ECOSIS) spectral catalog (Wagner et al., 2018). At runtime, we calculate an initial guess of surface reflectance using a band ratio water vapor retrieval as in Schläpfer et al. (1998). We then find the Euclidean-nearest Gaussian component to serve as the prior. This approach enables the retrieval to account for the unique reflectance statistics of vegetation and snow, which have overlapping absorptions in the near infrared range, producing consistent wavelength fits over heterogeneous terrain. To avoid biasing the reflectance magnitude, all prior means and covariances are rescaled to match the Euclidean norm of the initial guess as in Thompson et al. (2018b).

We perform the wavelength fit using a scene in North Africa (scene ID emit20220814t145733) with uniform substrate and topography that minimizes unrelated spectral variance. We average the data cube in the downtrack direction, reducing the image to a single row. We then fit the wavelength spline function independently to each spectrum, together with surface reflectance and atmospheric state variables. Departing from EMIT's operational atmospheric correction, we use a dense prior covariance which models cross-correlations between surface reflectance in all wavelengths from 380 to 2500 nm. This enforces reflectance smoothness in all channels to make use of atmospheric features across the full VSWIR interval. It also constrains the solution to be well-posed despite having many free parameters. The converged wavelength dispersion curve appears in Fig. 3. The pre-launch and post-launch wavelength calibration is nearly identical at 500 nm. The discrepancy is largest near 1900 nm where it reaches about −0.35 nm, or 2% of a channel width. We find no significant change in spectral response functions. The measured sampling of < 7.5 nm and FWHM of 8.5 nm significantly outperform mission requirements of 10 nm and 13 nm, respectively (Table 1).

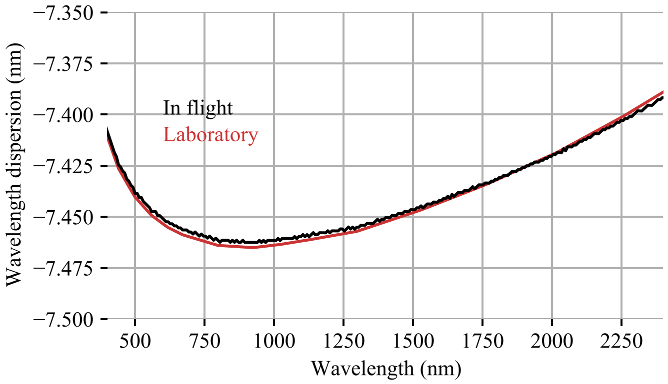

Fig. 3. EMIT Wavelength dispersion resulting from on-orbit and laboratory measurements.

2.2. Channel center wavelength uniformity

We next assess the spatial uniformity of the wavelength/channel assignments. As before, this process begins in the laboratory with the laser integrating sphere, by measuring the laser centroid at each cross-track location. Fig. 4 shows the result at 1949 nm, which is one of the more accurate lasers. A slight ripple in the measurement could be instability in the laser or other uncertainty in ground support equipment. The laser line centroids are consistent to within approximately 0.2 nm at all spatial positions, a uniformity of 98% in pixel units relative to a requirement of 90%. We assess the FPA clocking, i.e. the mechanical rotation of the detector in the plane of the FPA relative to the rainbow cast by the optics, using a linear fit shown in red. The best-fit line indicates the clocking even if the data itself are not perfectly linear. Here the line has no measurable slope, consistent with a properly-clocked FPA.

We perform a similar measurement on-orbit by fitting atmospheric absorption features. As before, the state vector includes parameters for center wavelengths and spectral response functions. However, this time, instead of representing center wavelengths with a multiparameter spline, we fit a single additive offset that shifts the wavelength axis. This simpler parameterization can be used with a restricted spectral range to repeat the experiment at multiple distinct absorption features. We fit the wavelength offset independently along with the surface and atmosphere

Table 1
EMIT Performance. SNR requirements are defined relative to a stressing case observation at 45 degrees solar zenith with a 20% surface reflectance. SNR requirements at other wavelengths are exceeded by a similar factor. We show the stray spectral response requirement for the region 5–81 channels from center, relative to peak response.

Parameter	Requirement	As measured
Spectral range	410–2450 nm	380–2500 nm
Spectral sampling	$<$ 10 nm	$<$ 7.5 nm
Spatial sampling	30–80 m	$\approx$ 60 m
Swath width	$>$ 1200 elements	$>$ 1240 elements
Spectral response (FWHM)	$<$ 13 nm	$<$ 8.5 nm
Channel wavelength uniformity	$>$ 90%	$>$ 98%
FWHM uniformity	n/a	$>$ 98%
Signal to Noise Ratio (SNR)	$>$ 190 at 700 nm	$>$ 500 at 700 nm
Stray spectral/spatial response	$<$ 0.002	$<$ 0.0001 corrected
Dark current drift	n/a	$<$ 1 DN / 12 h

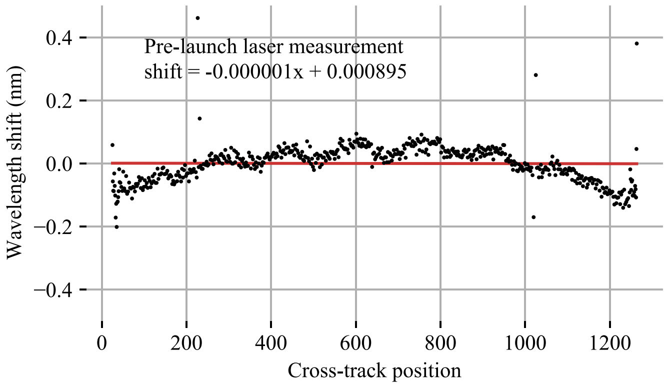

Fig. 4. EMIT FPA clocking before launch, measured in the laboratory with a laser source at 1949 nm. We report the shift as a linear trend in nm per pixel, plotted as a red line. (For interpretation of the references to colour in this figure legend, the reader is referred to the web version of this article.)

terms at each cross-track location.Fig. 5 shows the resulting on-orbit measurement of wavelength center deviation as a function of cross track position. The estimate is numerically very precise due to noise reduction from downtrack averaging and the large number of spectral channels that participate in the solution. Our empirical estimate of the measurement standard error, using the spread of the data relative to the best-fitting polynomial, is 0.008 nm, or approximately 0.1% of a channel width. Thus, the dominant errors in the calibration are likely to be systematic uncertainties in modeling of atmospheric absorption shapes. EMIT shows about 0.15 nm of spectral smile, apparent as a parabolic deviation in the wavelength center position. There is also an additional 0.1 nm of rotation, indicated by the slope in the red best-fitting line. This additional rotation is expected due to thermal cycles and the removal of gravity which moves the instrument components slightly from the laboratory configuration.

EMIT can dynamically adjust the FPA position by changing the temperature of its mounting components. We perform pre-launch tests to develop a thermomechanical model relating the component temperatures to the FPA position. This model predicts the temperature change to produce a desired FPA rotation. We have used the on-orbit clocking adjustments twice so far. The first time was in August 2022, when the FPA developed a small positive rotation after launch. We applied a new temperature setting and observed in subsequent atmospheric measurements that the rotation was removed. The second time was in January 2023 after the instrument had undergone a thermal cycle due to a temporary power outage. Here, the FPA showed a smaller rotation in the opposite direction (Fig. 5). This rotation was also corrected to near our measurement precision. (Fig. 6). These two tests demonstrate positional control on the order of 200 nm for an instrument of 300 mm in size. This precision would be similar to the length of a ping pong table if the spectrometer were the length of the continental United States. To our knowledge, this is the first demonstration of on-orbit FPA mechanical adjustments by an imaging spectrometer, and the most spatially-uniform alignment yet achieved for an instrument of this class. The center-to-peak shift of about 0.1 nm satisfies the most stressing measurement needs of future global spectrometers like SBG (Thompson et al., 2021).

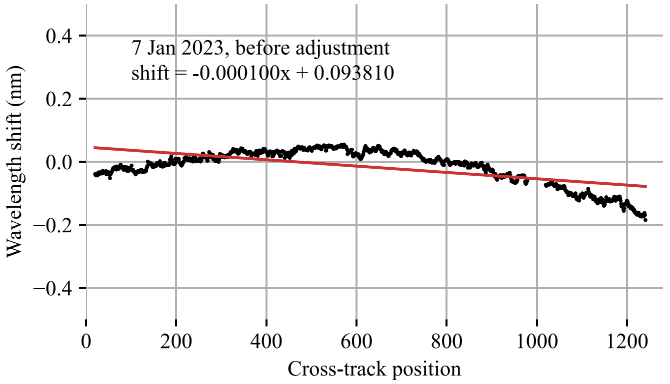

Fig. 5. EMIT FPA clocking after a thermal cycle (scene ID emit20230107t082602) but before on-orbit clocking adjustments. We measure the wavelength offset with atmospheric gas absorptions and report the shift as a linear trend in nm per pixel, plotted as a red line. (For interpretation of the references to colour in this figure legend, the reader is referred to the web version of this article.)

2.3. *Spectral response functions*

In addition to the wavelength center position, we characterize the spectral response function of each channel. This is typically taken to be Gaussian and constant across all spatial positions, but slight deviations are inevitable. To assess this parameter we first measure the pre-launch response functions in the laboratory. A monochromator sweeps a spectrally-narrow stimulus across all wavelengths in sequence. The rise and fall of this signal at a given channel indicates its Full Width at Half Maximum (FWHM).

We re-measure the spectral response functions after launch using the procedures outlined in Section 2.1, with a single parameter that expands or shrinks the FWHM at all channels. We do not find any significant differences beyond the original laboratory calibration, but when we perform this fit at all spatial positions, a small but measurable spatial nonuniformity appears. Fig. 7 shows a symmetric m-shaped curve in FWHM as a function of spatial position. This feature is consistent with laboratory data. The standard deviation of 0.16 nm is less than 2% of the FWHM, a level which is unlikely to be noticeable during most EMIT investigations. Consequently, EMIT processing uses a single spectral response function for each channel regardless of spatial position, an approximation which significantly simplifies science data processing.

2.4. *Stray spectral response*

The last spectral calibration activity measures non-Gaussian components of the spectral response function. Real instrument spectral response is non-Gaussian due to scatter from the grating and other optical elements in the spectrometer. In particular, the tails of the response function are slightly super-Gaussian. In the worst case this could cause distortions such as blurring of the spectrum and inaccurate retrieval of atmospheric parameters (Thompson et al., 2018a). The response of a single pixel is similar to the FPA image of a bright single-pixel source.

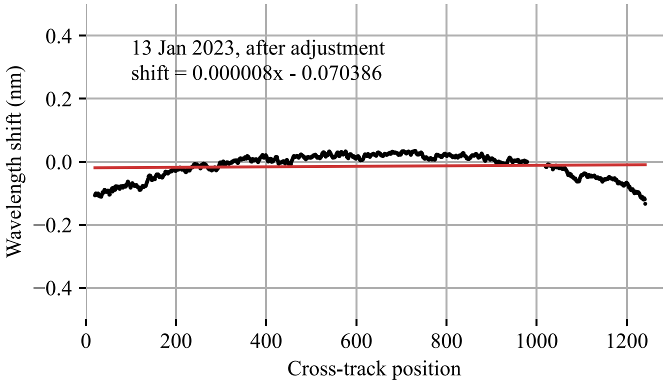

Fig. 6. EMIT on-orbit adjusted FPA clocking (scene ID emit20230113t053728) measured with atmospheric gas absorptions. We report the shift as a linear trend in nm per pixel, plotted as a red line. (For interpretation of the references to colour in this figure legend, the reader is referred to the web version of this article.)

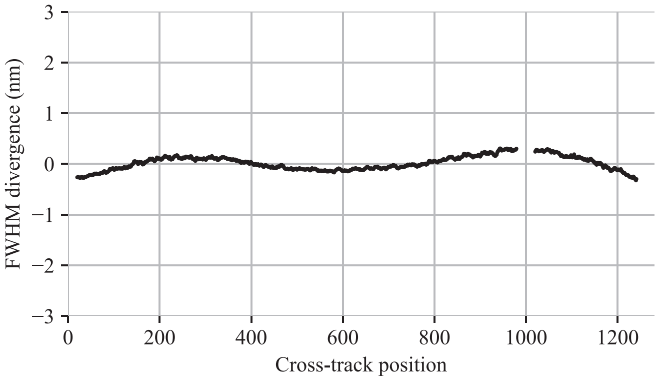

Fig. 7. Cross track deviation of SRFs, measured with atmospheric gas absorptions (scene ID emit20230107t082602).

This fact enables a laboratory measurement using spatial filters and a monochromator to produce a subpixel stimulus. We average a large number of frames to reduce noise and resolve the faint tail structure. We model the extra response with a set of concentric Gaussians. The model at position p uses the following form:

$$R(p,\mu,\zeta_1,\zeta_2,\zeta_3,\sigma_1,\sigma_2,\sigma_3) = \zeta_1 e^{-0.5(p-\mu)^2/\sigma_1^2} + \zeta_2 e^{-0.5(p-\mu)^2/\sigma_2^2} + \zeta_3 e^{-0.5(p-\mu)^2/\sigma_3^2} \tag{4}$$

where μ is the center position of the stimulus, σ_1 is the standard deviation of the central peak, and σ_2 and σ_3 are the standard deviations of the Gaussians forming the stray spectral response. The ζ terms are scaling coefficients on the Gaussian magnitudes. We fit free parameters to match the response function in logarithmic coordinates, with the cost function:

$$c(\mu,\zeta_1,\zeta_2,\zeta_3,\sigma_1,\sigma_2,\sigma_3) = \sum_{p\in\mathscr{P}} \left[log(x(p)) - log(R(p,\mu,\zeta_1,\zeta_2,\zeta_3,\sigma_1,\sigma_2,\sigma_3))\right]^2 \tag{5}$$

We fit these functions in both the spatial and spectral dimensions, scanning across all spectral channels $\mathscr{P}$ at a single field point.

Next, having measured these response functions at each FPA location, we develop a correction based on the linear deconvolution of Zong et al. (2006). We represent the blur as a matrix operator, with rows containing the stray spectral response. This operator multiplies the original spectrum to produce the additional blur. We define the measured radiance spectrum $\mathbf{L}_{obs}$ as a vector with dimensionality equal to the number of instrument channels n, the ideal radiance $\mathbf{L}_N$ as a vector representing the measurement in the absence of stray spectral response, and the true high spectral resolution radiance at aperture $\mathbf{L}_A$ with dimensionality m much greater than the number of instrument channels. We also define two sampling operators, a nominal Gaussian response matrix $\mathbf{H}$ of size $n \times m$, and a stray spectral response function matrix $\mathbf{G}$ of size $n \times n$, with spectral response functions on the rows of the matrix. We have:

$$\begin{aligned} L_{obs} &= GHL_A + HL_A + \varepsilon \\ &= GL_N + L_N + \varepsilon \\ &= [G+I]L_N + \varepsilon \\ &= AL_N + \varepsilon \end{aligned} \tag{6}$$

The matrix $\mathbf{A}$ contains stray spectral response functions (SSRFs) measured in the laboratory, with one added to the diagonal elements (Zong et al., 2006). To estimate the ideal channelized radiance from a blurred measurement we take the Moore-Penrose pseudoinverse $\mathbf{A}^+ = (\mathbf{A}^T\mathbf{A})^{-1}\mathbf{A}^T$ which enforces $\mathbf{A}^+\mathbf{A} = \mathbf{I}$. We multiply this correction operator with the original vector:

$$\widehat{\mathbf{L}}_{obs} = \mathbf{A}^+\mathbf{L}_M \tag{7}$$

We perform this procedure independently in spatial and spectral dimensions, resulting in two matrix operators applied independently at runtime to correct the EMIT data.

Fig. 8 shows an example. The top panel shows spectral correction of a laboratory monochromatic source held out of the fitting procedure. The original response appears in red. Our correction recovers the ideal Gaussian response, a parabola in logarithmic coordinates (in black). The bottom panel shows the spatial correction. Even without software correction, deviations from Gaussianity are almost three orders of magnitude below the peak, outperforming mission requirements for stray response (Table 1). This is considerably better than many historical grating-based instruments like NASA's Next Generation Airborne Visible Infrared Imaging Spectrometer (AVIRIS-NG) (Thompson et al., 2018a). We attribute this improvement to a new grating designed explicitly to reduce scatter. After the software correction, deviations are no longer measurable in laboratory data.

Validating the improvement on remote reflectance retrievals is more challenging, since the magnitude of the correction for EMIT is small and the differences are easily masked by changes to the retrieved atmospheric state. We look to the water vapor feature at 1800–1900 nm, where absorption is so strong that the lower troposphere is effectively opaque to remote instruments. These radiance channels should contain only noise that is decorrelated from the surface reflectance signal. Any visible evidence of surface features in these channels represents unwanted spectral scatter from neighboring bands. To assess this effect, we extract a rectangular region approximately 20 × 20 km from an arid-land scene, with high-contrast features that show a range of surface albedos (scene ID emit20220807t183301). The image of the absorbed channel at 1841 nm shows some weak evidence of features from the surface at a level close to the noise. The correlation coefficient with the

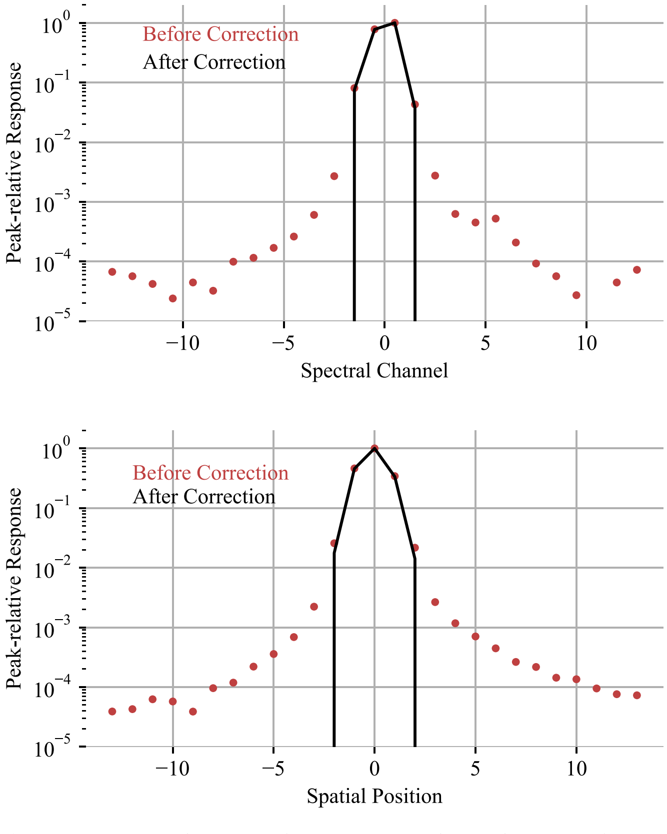

Fig. 8. EMIT spectral response function (top) and spatial response function (bottom), before and after correction for stray response.

neighboring unabsorbed channel at 1744 nm is 0.29. After the SSRF correction, surface features are nearly imperceptible and the correlation coefficient drops to just 0.13, evidence that the spectral response correction is successful.

3. Radiometric calibration

EMIT's radiometric calibration maps the intensity of the sensor response, expressed in instrument digital numbers, to radiance at aperture in units of μW nm^{-1} cm^{-1} sr^{-1}. Fig. 9 shows the steps in the procedure, which includes replacing nonfunctional detector elements in the FPA and correcting any optical artifacts such as ghosts. We discuss each of these operations in the following sections.

We use a linear model of the observed radiance L_{obs} with a zero point d_0, gain factors ν, and digital number measurement d. The radiance is a function of FPA row r and column c:

$$L_{obs}(r,c) = \nu(r,c)[d(r,c) - d_0(r,c)] \tag{8}$$

We further decompose the gain factors ν into radiometric calibration coefficients, one per channel, and a flat field image representing spatial nonuniformities in radiometric response. The detector response is linear over the relevant dynamic range within the error of the laboratory measurements, so we do not apply any linearity corrections to the data.

3.1. Zero point estimation

The first step of the calibration finds the zero point for each FPA element. The zero point is the Digital Number (DN) corresponding to zero illumination. It changes on different timescales due to varied effects such as the thermal dark current and electronic phenomena. We measure the long-timescale changes with an image of a dark scene from the same orbit as each EMIT science image. We take the temporal median of dark frames to find a dark measurement d_k. The dark-subtracted frame is:

$$d_{ds} = d - d_k \tag{9}$$

The EMIT instrument has no shutter, so we acquire dark frames over the non-sunlit side of the Earth. It is important that these scenes be truly dark, without city lights or aurora. EMIT has a large dynamic range, and sources 200,000 times weaker than the solar-reflected signal would cause contamination commensurate with instrument noise. To prevent contamination, we create a global mask of regions on Earth that are dark at nighttime. We average VIIRS Day/Night Band (DNB) global mosaics over 10 months, and remove any areas within one swath width of terrain that could contain city lights. We also mask out illuminated ocean areas with nighttime fishing activity or aurora. We further subset the resulting area to remove areas in twilight where the sun is less than 20 degrees below the horizon. The remaining ocean surface is used for dark acquisitions. We ignore moonlight when scheduling dark acquisitions since the modeled signal from a full moon is below the instrument noise. Analysis of over 1000 EMIT dark acquisitions confirms this prediction, showing no measurable correlation between lunar phase and dark signal level.

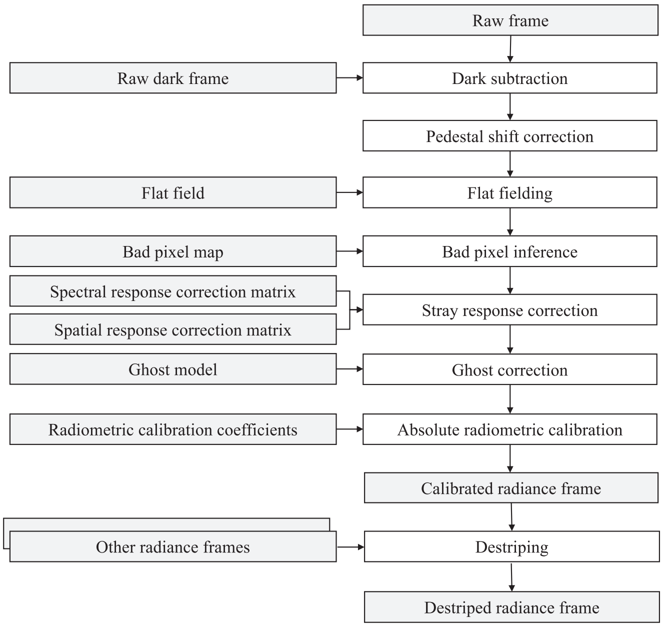

Fig. 9. Radiometric calibration procedure. Grey boxes correspond to data inputs, white boxes to procedures.

The dark level naturally drifts over time with any FPA temperature changes. The EMIT instrument addresses this with active cooling to hold the FPA at a stable cryogenic temperature. To assess the dark current drift rate, we compare measurements on the non-sunlit side of the Earth spaced approximately 12 h apart. The dark drift shows a bimodal distribution, with one population of pixels drifting higher and another drifting lower. The average drift is -0.16 DN over the 12 h period, with a standard deviation of 0.67 DN. This is an order of magnitude below other noise sources. It is a conservative estimate of drift-related errors because EMIT acquires dark measurements in the same 90 min orbit as the associated science data, rather than 12 h apart. We conclude that radiometric error induced by dark drift is negligible.

We must also account for electronic processes that occur on faster timescales. *Pedestal shift* in illuminated FPAs appears as a residual error in the zero point after the dark frame is subtracted, and can differ for each spectrum. We estimate this residual using several rows and columns at the periphery of the array that are blocked from external illumination. We analyze the masked rows and columns of each dark-subtracted frame, defining $d_m(c)$ to be the median of the masked rows in d_{ds} at column c.

$$d_q(r,c) = d_{ds}(r,c) - d_m(c) \tag{10}$$

Similarly, $d_n(r)$ is the median of masked rows in d_q at row r. The zero point is:

$$d_0(r,c) = d_k(r,c) + d_n(c) + d_q(r) \tag{11}$$

Subtracting d_0 from d shifts the digital number scale so that numerical zero corresponds to radiometric zero.

3.2. Detection and repair of inoperable pixels

The next step of radiometric calibration replaces inoperable pixels in the FPA. We deal with two kinds of inoperable pixels: permanently inoperable detector elements; and elements that are unusable in the current frame because they are saturated by bright illumination. We identify permanently inoperable elements in laboratory data by flagging locations that are either (a) stuck on a single value, or (b) have a noise standard deviation which is different from the population of normal pixels. Inoperable pixels are easy to spot visually, since they appear as spikes in the otherwise smooth DN curves of laboratory broadband sources. A manual assessment found several additional pixels that did not trigger our statistical criterion. At the time of launch, 1007 pixels out of EMIT's 419,840 were unusable, an operability rate of 99.8%.

In addition to inoperable pixels, we also detect and replace saturated FPA elements of each frame. Bright targets such as snow at high solar elevations occasionally fill the detector well capacity. EMIT has a short integration time mode that can limit the photon flux when bright targets are anticipated. However, we rarely use this mode since it reduces radiometric sensitivity. Moreover, predicting saturation in advance is inconvenient for clouds, specular surfaces, or seasonal snow cover. Thus, it is common for images to contain a small fraction of pixels with saturated channels. We detect these channels based on their DN counts and flag them as additional bad pixels for replacement.

Our replacement algorithm follows Chapman et al. (2019). We find a statistically appropriate replacement for each pixel based on the most similar pristine spectrum in that frame (i.e. a 1242-pixel line of image data from a single integration time). We find the most similar spectrum with a spectral angle metric (Kruse et al., 1993) and fit a linear model mapping the values from the pristine to the incomplete spectrum. We use this linear relationship to predict the missing pixels. Fig. 10 applies the replacement process to a laboratory source. The replacement strategy preserves spikes at 650 and 1290 nm from the order sorting filter seams, and removes spikes at 820 and 900 nm caused by bad pixels. A manual survey of images acquired after launch determined that no additional bad pixels had appeared in the FPA, so no on-orbit update of the bad pixel map was necessary. Fig. 11 shows replacement of saturated channels in a flight spectrum. We use unsaturated cloud pixels in the scene to calculate a statistically appropriate interpolant that is indistinguishable from a physical cloud spectrum. Since these values are inferred rather than measured, analysts may wish to downweight them in surface analyses. The EMIT radiance data products include a mask indicating which channels of each spectrum have been replaced.

The order sorting filter boundary at 1290 is particularly difficult to calibrate; its spectral response function and radiometric sensitivity vary across different acquisitions and substrates. However, this filter seam is “bad” for all spectra in the frame, so we cannot fix it using the Chapman et al. (2019) approach. Instead, we interpolate the radiance over the three affected channels using cubic interpolation, and mark these locations as having high uncertainty for the downstream processing. Atmospheric correction approaches capable of using this information can downweight the bad channels appropriately in the reflectance solution.

3.3. Radiometric flat field

The third stage of radiometric calibration transforms instrument DNs to units of radiant energy. The transformation is different for every pixel on the FPA. For convenience, we decompose it into two parts: a flat field, representing spatial variability of the FPA response; and a vector of radiometric calibration coefficients, representing a channelwise translation from digital numbers to radiance units. We first measure the flat field in the laboratory by sweeping a source with constant illumination laterally across all FPA elements. We characterize the signal’s rise and fall at each FPA element independently, fitting a six-degree polynomial in the time domain. The peak of this polynomial indicates the “hot spot,” the maximum signal seen by the FPA element. By repeating this operation at every FPA location, we find the FPA response as if the field were spatially uniform, even though the calibration source contains spatial structure. We estimate the flat field from these values by calculating the average digital number in a reference region of the FPA. We define the reference region using several hundred FPA columns at the one and two-thirds field positions. We then calculate the average DN value in these reference columns independently for each channel, and normalize each FPA element’s response by this reference to produce the flat field.

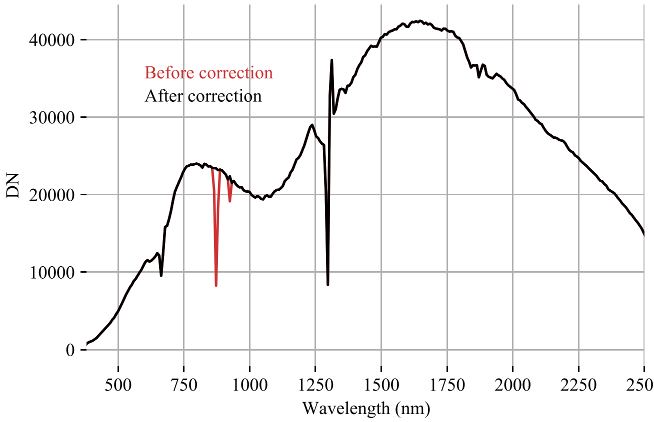

Fig. 10. Procedure for replacing inoperable pixels. The spikes at 650 and 1290 nm are due to order sorting filter seams, which are correct. The spikes at 820 and 900 nm are caused by bad pixels. The replacement strategy effectively removes the artifacts.

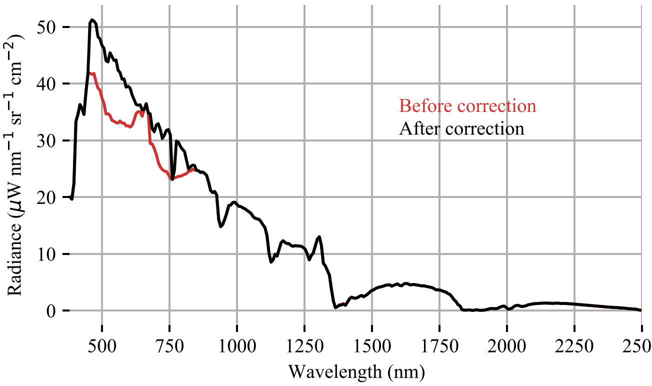

Fig. 11. Procedure for replacing saturated pixels. An EMIT cloud radiance spectrum is saturated in channels brighter than about 40 μW nm^{-1} sr^{-1} cm^{-2}. The replacement values obey the statistics of cloud spectra in the same frame.

The flat field can change over multiple spatial and temporal scales. Over short timescales, electronic drift can change the gain of each FPA element. Such changes manifest as small shifts in the sensitivity of different FPA elements or columns. Over long timescales, physical degradation or contamination of optical components can cause spatially-broader changes. Even sub-percent errors in relative radiometry can create visible artifacts in downstream data products. Consequently, we update the laboratory flat field on-orbit. Our first update aims to capture any spatially-broad changes in instrument sensitivity that occur between laboratory tests and on-orbit comissioning. We achieve this by averaging over 1600 radiance images from the first weeks of operations. We exclude from this average any pixels which fail the EMIT reflectance quality criteria due to the presence of clouds or water. We then normalize each frame of data independently by dividing out the mean spectrum. The resulting flat field update shows clear changes in visible wavelengths, but only ambiguous differences in longer wavelengths. Thus, our post-launch update only modifies visible wavelengths less than 550 nm. Fig. 12 shows the impact of this update on an EMIT scene over the Caspian sea. A blue band at the two thirds position disappears after the change.

Even after the post-launch flat field changes, minor column-to-column differences persist. This variability at the 0.1% level is most likely related to drift in electronic state of the detector amplifier circuits

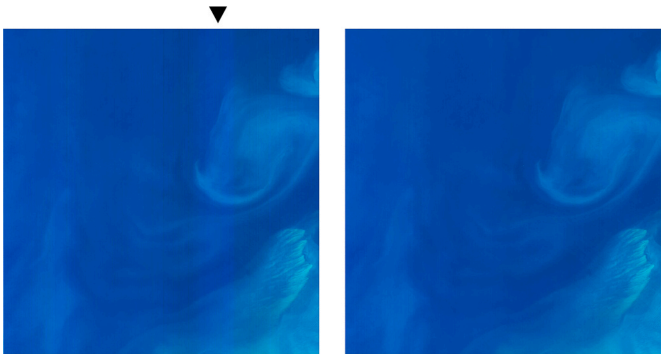

Fig. 12. Caspian sea (scene ID emit20220815t042814). Left: Original EMIT image, RGB channels. A black arrow indicates a vertical banding artifact. Right: After post-launch flat field update.

over shorter timescales. It appears visually in images as subtle vertical stripes. To capture these high spatial frequency differences we calculate updates to the flat fields for specific time segments. Early in the mission, we tried fitting a separate flat field to each image with a statistical destriping algorithm described in Chapman et al. (2019). It worked adequately for most images, and was used in the first few months of EMIT data processing. However, we found that very strong vertical image edges could distort the flat field. To remedy this, we developed an alternative approach using longer temporal averages as in Green et al. (2011).

Our procedure considers all images in a small temporal interval around the scene to be corrected. We use a three day window for EMIT, which provides hundreds of independent images. The first step uses spatial filtering to identify homogeneous areas within each image. Specifically, we run a Sobel edge detector followed by morphological dilation to mask out areas near strong contours. This, and a threshold to remove the brightest pixels, prevents clouds and edges in scene content from influencing the flat field. Second, we take the median of remaining pixels in the downtrack dimension as a robust estimate of the average frame for each image. Third, we filter these average frames using a high-pass spatial filter in the cross-track direction, revealing high spatial frequency variability between neighboring columns. Fourth, we create image-specific flat fields by ratioing FPA rows by the radiometric reference area of the FPA. Individual image-specific flat fields can still be influenced by measurement noise and scene content, so we combine them in a temporal median over the entire three day window for a robust estimate. For convenience, we apply this update as a multiplicative factor to each radiance image in postprocessing. This approach may lead to inaccuracies, since the original flat field operation comes before optical corrections in our calibration workflow. However, the magnitude of these updates is so small (on the order of 0.1–0.3%) that any approximation error is negligible.

Fig. 13 shows the effect of the flat field update on a typical EMIT image. The left panel shows three channels of a Minimum Noise Fraction (MNF) transformation, a change of basis designed to identify independent signals in the image. This representation, similar to Principal Components Analysis, tends to accentuate systematic noise and reveal vertical striping artifacts. Here, we show MNF bands 4–6, where significant vertical striping is present. The right panel shows bands 4–6 from a second MNF transformation after the updated flat field has been applied. The flat field updates improve radiometric uniformity to a level at which it should not have a major impact on EMIT's mineral mapping objectives. Fig. 14 shows the magnitude of this update as a spectrum at a single field position. Flat fields compared with the difference of a single day are typically consistent to within 0.1%. After ten days, the gains have drifted a bit more, but are still generally within 0.2%. This suggests that the flat fields contain information about the average gain drift of EMIT's FPA. To quantify this drift, we fit a semivariogram to several hundred independent FPA pixels over a timespan of two months. The semivariogram quantifies the differences in any FPA element as a function of time lag. The square root of the semivariogram, plotted in Fig. 15, shows the expected drift in pixel sensitivities over time. The median drift in sensitivity is approximately 0.1% over a month. However, in the same timespan, each spectrum is likely to contain channels that drift by up to 0.25%. These levels are significant enough to explain the visual striping. This underscores the value of continual flat field updates to track detector changes and ensure visual uniformity of EMIT data products.

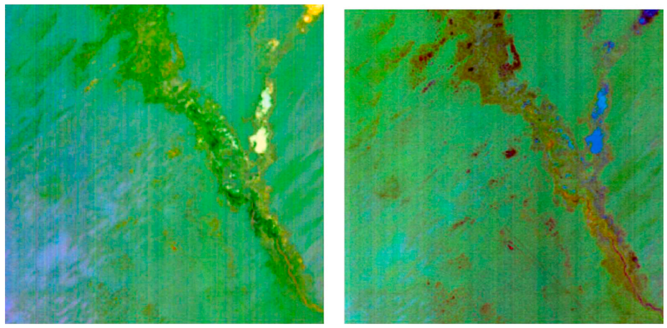

Fig. 13. Arid scene (scene ID 20220828 t051941). Left: Original EMIT image, MNF Bands 4–6, constrast stretched. Right: After daily flat field update. RGB colour assignments are arbitrary.

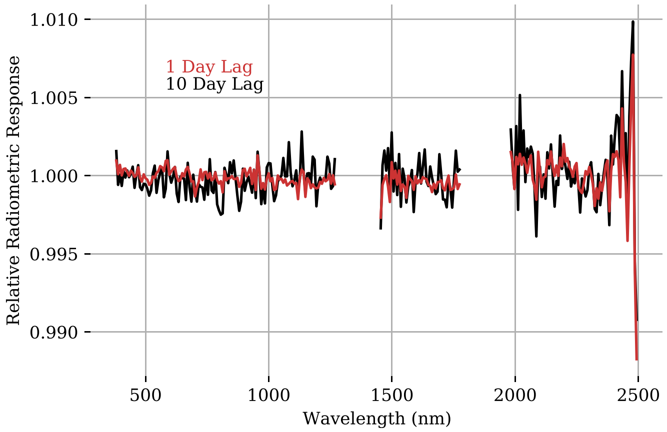

Fig. 14. Example column of the flat field update showing how a single field position varies in sensitivity over one and 10 day intervals.

3.4. Optical ghosts

EMIT's Dyson design creates structured stray light artifacts known colloquially as ghosts. The most significant ghost comes from an unwanted reflection from the detector that travels to the grating and back to the opposite side of the FPA. It appears as a blurred and spectrally scrambled image of the original signal. Fortunately the effect is consistent and correctable. We follow the correction approach of Zandbergen et al. (2020). We first identify the axis of symmetry ψ, the cross-track pixel location which ghosts onto itself. For cross-track pixel positions indexed starting at zero on the left side of the array and incrementing toward the right, a pixel at location i ghosts onto a location j given by $j = 2^{*}\psi - i$. This allows construction of a ghost image for any scene using nearest-neighbor sampling. To find ψ, we acquire a laboratory scene with a spatially-localized source to clearly show the original and ghost features on opposite sides of the FPA. We then optimize ψ to maximize the sum of element-wise products between the ghost image pixels and the originals. The spectral structure of the ghost and original are

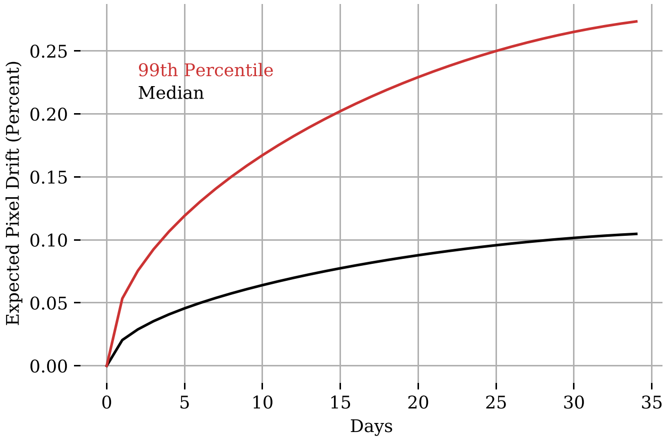

Fig. 15. Flat field drift over time.

different, but we find that ψ is effectively the same for all wavelengths. We perform this analysis independently on each channel and use a robust median to find the axis of symmetry.

Next, we define a sparse Ghost Location Matrix (GLM) that describes the mapping of source wavelength channels to ghost channels on the opposite side of the FPA. Here, the term “channel” refers to position along the spectral dimension of the FPA, indexed starting at zero with the longest wavelengths at the top, and incrementing toward shorter wavelengths at the bottom. The GLM is identical at all spatial positions, so we only need to determine it once. We sweep a strong subpixel source across the EMIT wavelength range using a monochromator, and measure the channel position of the ghost reflection on the opposite side of the FPA. Fig. 16 shows the resulting channel to channel mapping. Red lines show robust linear fits to each ghost order based on the RANSAC algorithm (Fischler and Bolles, 1981). Often, the signal from a single source wavelength is spread across multiple channels in the ghost reflection, so careful digital rasterization is needed.

Each channel has a different ghost magnitude based on the efficiency of the grating and the other components along its optical path. We measure these intensities with bright spatially-extended broadband sources similar to the illumination observed on-orbit. We illuminate just one side of the FPA so that both source and ghost can be measured independently. Several different source channels can project onto the same ghost channels. For example, in Fig. 16, ghost channel 200 is a combination of reflections of four different orders coming from different wavelengths in the source spectrum. To resolve this ambiguity, we measure the stimulus and ghost spectra of over 20 different spectrally-distinct sources attenuated by different broadband filters. This collection of spectrally-diverse stimuli leads to an overdetermined system of equations to find the ghost reflection efficiency coefficients. To reduce the number of unknowns in this system, we manually split each linear reflection order in the GLM (i.e. the red lines in Fig. 16) into piecewise linear intensity profiles. A final blurring operation, based on a concentric Gaussian kernel, blurs the ghost image in spatial and spectral dimensions. The parameters of the blurring operator are optimized together with the slopes and offsets of the intensity segments via gradient descent to zero out the ghost features in the spectrally-diverse training set.

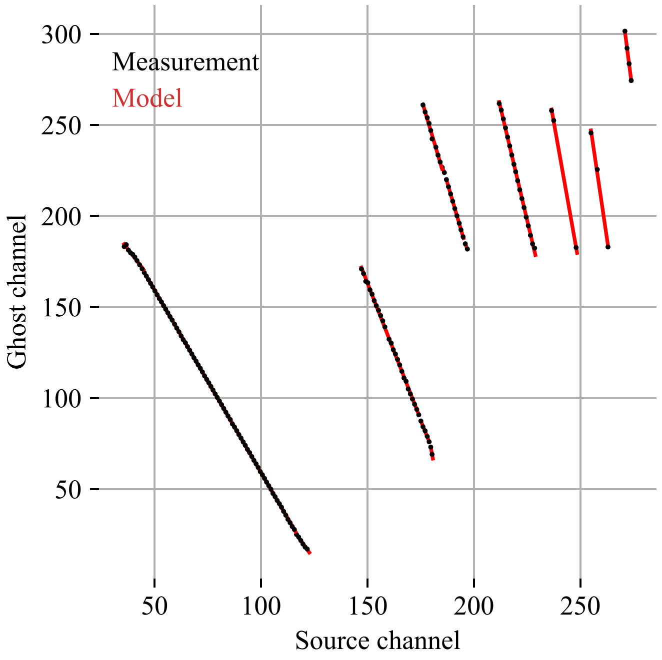

Fig. 16. Ghost Location Matrix (GLM). The horizontal axis shows the original channel of the stimulus, while the vertical axis shows the position of the ghost. Often multiple source channels project onto the same ghost channel. Each channel has a different and unknown ghost intensity.

To summarize, the complete ghost model consists of: the axis of symmetry; the GLM; an intensity associated with each nonzero GLM element, defined as a piecewise linear function of source channel number; and the bandwidth of the final blurring operator. After fitting these parameters, we use this description to predict the reflected ghost image for any new observed scene. We then subtract the ghost image from the original to remove the stray signal. The procedure is slightly circular in that the signal used to predict the ghost image itself contains some ghost photons. However, the ghost intensity is less than 1% of the signal, so the resulting error is vanishingly small. Fig. 17 shows the result of the ghost correction procedure on a held-out laboratory source. The ghost appears as a bright stripe opposite the true source. The correction procedure erases this stripe. Fig. 18 shows the associated ghost spectrum before and after the correction procedure. The ghost correction appears to work equally well in flight data; the only residual discovered so far in a year of operations is a small (1–5 DN) signal observed occasionally from 2000 to 2500 nm in perfectly absorbing surfaces such as sunglint-free water. In radiance terms this is approximately 0.0005 μW nm^{-1} cm^{-2} sr^{-1}, more than three orders of magnitude below the water-leaving reflectance signal.

3.5. Radiometric calibration coefficients

We represent the multiplicative translation from DNs to radiance units as a vector of *Radiometric Calibration Coefficients (RCCs)*. We measure RCCs in the laboratory by illuminating a reflective panel with a source of known intensity and geometry, and calculating the resulting radiance at sensor. Our calibration source is a NIST-traceable broadband lamp. The radiance prediction incorporates the known transmittance of other optical components in the chain, such as the reflectance of a fold mirror and the transmittance of a window into the vacuum chamber containing EMIT. Since much of the optical chain is outside the chamber in free air, the radiance measurement is also subject to atmospheric gas absorption. The primary absorbing gas is water vapor, which has prominent absorption features at 1380 and 1880 nm. We address this by interpolating radiometric calibration coefficients spectrally across the contaminated intervals.

We update radiometric calibration coefficients on-orbit for several reasons. First, the instrument sensitivity can change over time as the FPA ages, and to a lesser degree between thermal cycles as the FPA accumulates trapped charge. Additionally, the instrument noise level, which is a small fraction of 1% of the signal for most targets, is always smaller than systematic errors in our laboratory calibration, so there will always be a need for refinement. Finally, the laboratory sources used for radiometric calibration have lower levels of blue illumination than the sun (Helmlinger et al., 2016), so any out-of-band response in short wavelength channels can induce radiometric error when applying the calibration to flight data.

For these reasons, we adjust the radiometric calibration coefficients on-orbit using a vicarious reference target measured by a ground team with a field spectrometer. We follow the procedure outlined in Bruegge et al. (2021), which predicts the radiance at sensor and then uses the ratio with actual measurement to derive a radiometric calibration

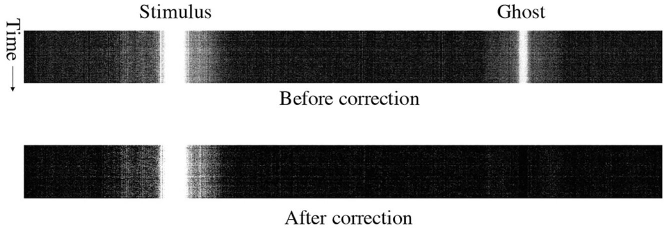

Fig. 17. Ghost correction procedure. We predict the ghost associated with the measured image, and then subtract it from the original.

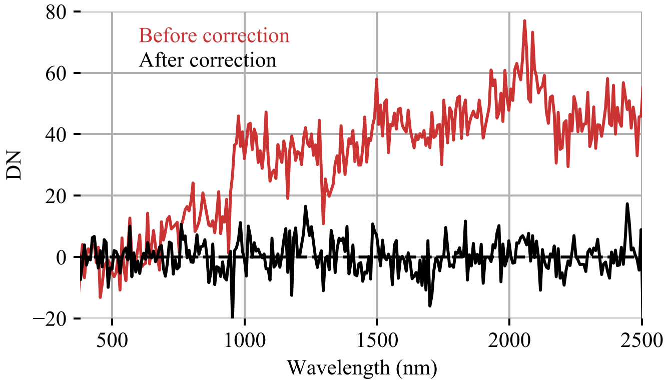

Fig. 18. Ghost signal, before and after correction procedure.

update. VSWIR imaging spectrometers are sensitive to small changes in atmospheric water vapor (Richardson et al., 2021), so reanalysis models are not sufficient. Instead, we retrieve the atmospheric aerosol and water vapor from EMIT data itself, along with the surface reflectance at the measured location, following the approach of Section 2.1. However, we now fix the instrument parameters to their calibrated values. We also retrieve pressure elevation as in Thompson et al. (2015), by adding it to the state vector of variables that are optimized to fit the radiance spectrum. This helps obtain a more accurate Rayleigh correction, which is critical for radiometric calibration of visible wavelengths. We used data from Black Rock Playa (40.984 N, 118.9675 W, Fig. 19 Left), a large homogeneous playa area in Nevada, USA. The EMIT overflight took place on 18 August 2022 at approximately 21:00 h UTC (scene ID emit20220818t205752). The remote measurement estimated the atmospheric water vapor content as 2.27 g cm^{-2}. Conditions were cloud free with an aerosol optical depth of 0.11 at 550 nm. Then a field team measured the same playa on 21 August at the same time of day (Meyer et al.,2023a, 2023b). The field team used a leveled spectralon panel as a reflectance standard, and acquired spectra with continuous traverses across a 240 × 240 m area of the southwest corner of the playa. The average spectrum of the area is corrected for the absorption of the reference panel and minor offsets between detectors in the field spectrometer, and mathematically resampled to EMIT spectral characteristics. We use the remotely-measured atmospheric model to transform the in situ spectrum to a top of atmosphere radiance. The complete atmospheric description is a MODTRAN model that includes estimated water vapor and aerosol values as well as all other major gases with absorption in the VSWIR spectral range, following Thompson et al. (2021). Finally, we calculate the change in radiometric calibration coefficients which would have caused the target spectrum to be measured. Uncertainties in this process include errors in the bidirectional reflectance of the reference panel, which impact the in situ measurement, and inaccuracies in the atmospheric model, which impact the predicted radiance. To mitigate these errors, we perform this adjustment in clear sky conditions and assess the update carefully with validation sites.

To validate the radiometric update, we apply the new calibration to other locations where ground truth spectra are available. We first test an in situ spectrum from the RadCalNet automated test facility at Railroad Valley, Nevada, 38.504 N, 115.692 W (Bouvet et al., 2019). The center panel of Fig. 19 shows the Playa surface. The in situ spectrum has near perfect temporal coincidence to EMIT. We extract the EMIT data from this image location, averaging a 3 × 3 pixel window around the facility to mitigate the impact of single-pixel variability or spatial sampling uncertainty on the result. We then estimate its reflectance. Fig. 20 shows the result; the top left panel shows the remote measurement in black, and the in situ data in red. We blank out wavelengths above 2300 nm that are not measured by the in situ spectrometer, and intervals in the shortwave infrared which are opaque due to atmospheric absorption. The bottom left plot indicates the difference, underscoring the close agreement between the remote and in situ data under optimal observing conditions. Outside the deep water absorption features at 1380 nm and 1880 nm, the mean absolute difference is just 0.7%. The largest discrepancies at short wavelengths may be residual calibration error, perhaps caused by aerosol interference during the vicarious calibration. Alternatively, it is possible they are caused by atmospheric modeling errors in the Railroad Valley spectrum. Other departures at 1500 nm and 2100 nm may be related to uncertainty in atmospheric modeling of gaseous absorption by water vapor and CO_2.

We perform a second ground-validation experiment at Smith Creek, Nevada (39.326 N, 117.446 W, Fig. 19 Right) The result appears in Fig. 20, Right. This site was measured approximately two days earlier than the overflight, but about four hours earlier in the day, using the same protocols as Black Rock Playa (Meyer et al., 2023b). The difference in acquisition time, resulting discrepant illumination and change in the bidirectional reflectance, may account for the larger 2.2% mean absolute difference observed at this location. Nonuniformity in the playa surface might also play a part. Nevertheless, the shortwave infrared mineral features of the playa surface are captured in the remote data.

3.6. *Instrument noise performance*

We predict instrument noise with a comprehensive radiometric model of the optical system. EMIT has a simple layout (Bradley et al., 2020) with a two mirror aluminum telescope and a Dyson imaging spectrometer (Fig. 21). The telescope focuses incoming light on a black carbon 30 μm-wide slit at the spectrometer interface. The spectrometer itself uses a calcium fluoride lens and a custom-fabricated grating produced by the Jet Propulsion Laboratory Microdevices Laboratory (Mouroulis et al., 1998). Its detector is a 480 × 1280-format cryogenic Mercury Cadmium Telluride array from Teledyne Technologies Inc., of similar design to their CHROMA series (Sullivan et al., 2017). During operation, 328 channels of this array are used. Our radiometric model incorporates component-wise predictions of optical efficiency, along with noise predictions for the signal chain and detector operating at

Fig. 19. Playas used for radiometric experiments. Right: Black Rock Playa. Center: Railroad Valley Playa, courtesy Carol Bruegge. Right: Smith Creek Playa.

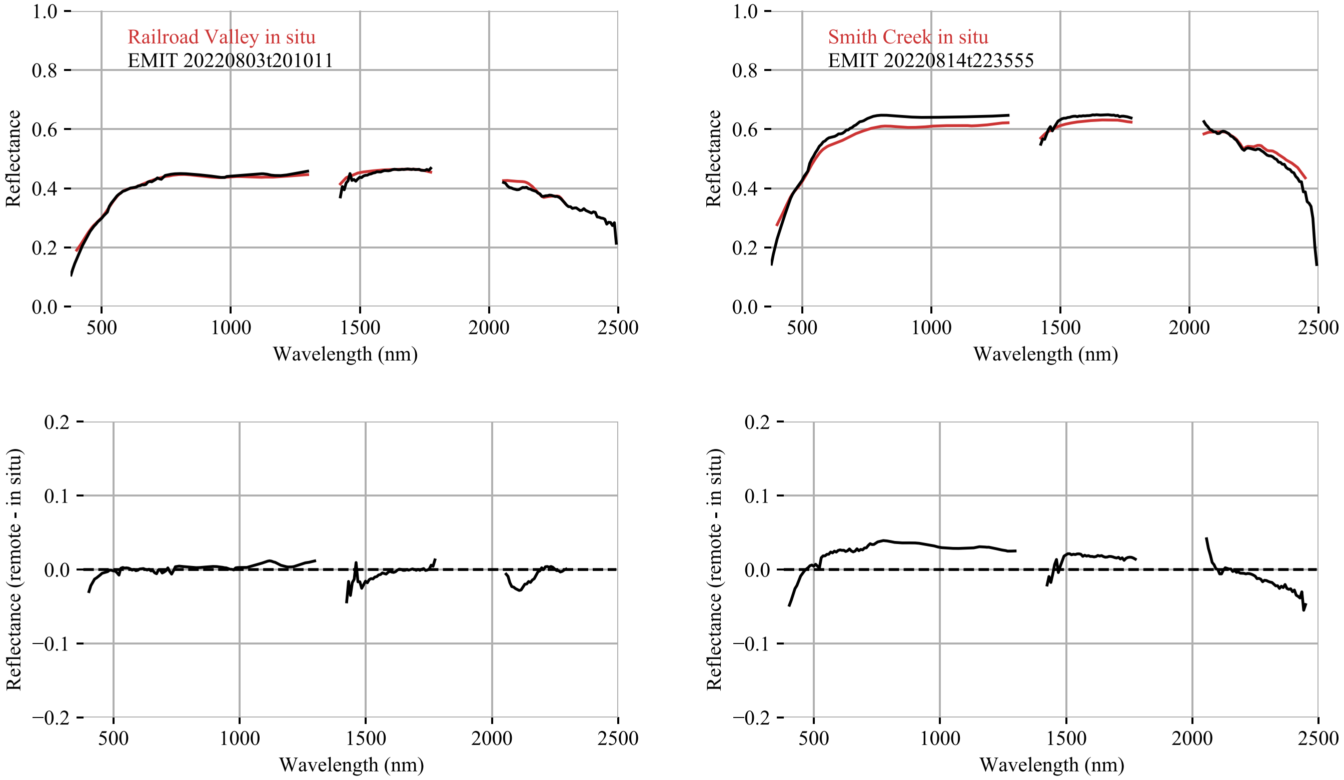

Fig. 20. Reflectance comparisons of remote and in situ spectra at the Railroad Valley automated site (Left) and Smith Creek manual site (Right). The Railroad Valley spectra were nearly simultaneous, while the Smith Creek acquisitions differed in their time of day.

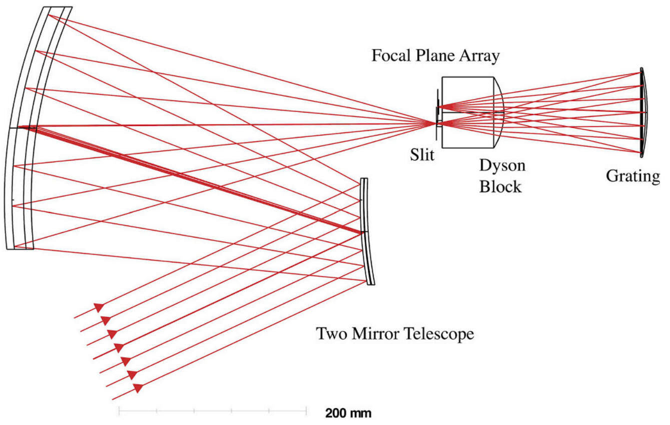

Fig. 21. EMIT optical layout. Red lines illustrate light pathways, and instrument components are in black. A two-mirror telescope images incoming light onto a slit that limits the field of view to a line across the Earth's surface. Light then passes through the Dyson lens, is spectrally dispersed by the grating, travels back through the same Dyson lens, and finally intersects the focal plane array detector. (For interpretation of the references to colour in this figure legend, the reader is referred to the web version of this article.)

cryogenic temperatures.

The total noise σ_{tot} is a function of scene radiance L_{obs} given in μW cm^{-2} sr^{-1} nm^{-1}.

$$\sigma_{tot} = \frac{\sqrt{\sigma_p(L_{obs})^2 + \sigma_d^2 + \sigma_q^2 + \sigma_r^2 + \sigma_e^2}}{\sqrt{2}} \tag{12}$$

Where σ_d represents dark current noise, σ_q quantization noise, σ_r read noise and σ_e electronic noise. $\sigma_p(L_{obs})$ is the photon shot noise, the standard deviation of photons arriving during the integration time. EMIT spectra are the combination of two sequential integrations coadded by the FPIE-D to make a single pixel. Noise is independent over time, so this reduces the noise of each spectrum by $\sqrt{2}$. The expected number of photons reaching the detector during each integration time is given by:

$$\sigma_p(L_{obs})^2 = 10^6 L_{obs} E^{-1} t_{int} \Delta_{chn} a_\omega T \tag{13}$$

with photon energy E of hc/λ Joules, where h is Planck's constant and c is the speed of light in a vacuum. The integration time is t_{int}, and the effective channel width in nanometers is Δ_{chn}. The symbol T represents the total instrument throughput, including the losses due to the grating, filters and mirrors, and the quantum efficiency. The symbol a_ω is a function of detector area a_{det}, and the instrument F number:

$$a_\omega = \frac{1}{4} a_{det} \pi F^{-2} \tag{14}$$

We form the original radiometric model from laboratory measurements of component efficiencies. On-orbit, we update the noise estimates using measurements of dark scenes, which suggest about 7.5 DNs (approximately 155 electrons) of noise in the absence of illumination. This is better than laboratory predictions of over 200 electrons. We also incorporate updates in radiometric calibration coefficients, bookkeeping them as changes to the instrument transmittance T. Thus revised, the model can predict the noise for new scenes.

Validating radiometric performance requires measuring noise in illuminated scenes, which is challenging due to natural variability in surface cover. Traditionally, analysts estimate instrument noise over spatially uniform playas or deserts. Over truly uniform surfaces, any differences between neighboring pixels are instrument noise (Boardman and Kruse, 2011). However, even the most homogeneous locations on Earth appear variable at EMIT's sensitivity and spatial resolution. Consequently, we need a new procedure for assessing noise. We begin with a scene that is as homogeneous as possible, and model the remaining spectral variability using a low-rank Principal Component (PC) representation. We manually select the number of components based on the eigenvalue at which an image-space projection of that coefficient degrades to spatially-decorrelated noise (Asner et al., 2012). We treat this PC projection as a de-noised image, and subtract it from the original dataset to produce an image of "noise spectra." Some real noise appearing in the first components is artificially removed by this subtraction. However, instrument noise is typically isotropic and independent in each of the 285 channels, so any bias due to removing a handful of dimensions is on the order of 2% or less. We estimate measurement error using the sample covariance of this noise image. We analyze a homogeneous patch of the Caspian Sea as a dark scene dominated by read and electronic noise. This open-water scene contained three eigenvectors of scene signal. We also consider a large patch of the USGS Libya 4 calibration site (Mishra et al., 2014) as a bright scene dominated by photon shot noise. It contained six eigenvectors of scene signal.

Fig. 22 shows the result. The measured noise levels lie within about 10% of the model predictions for both dark and bright scenes. The departures are largest in the darkest regions of the spectrum, such as the opaque water vapor features at 1880 nm, suggesting the constant noise terms may still be too pessimistic. Fig. 23 translates this noise level to an SNR for the median Libya spectrum. SNRs are above 500 in most regions of the spectrum, and above 750 in most of the visible-near infrared. The SNR is balanced across wavelengths, reflecting design decisions that allocated grating efficiency to measure features across the entire spectrum: the visible electronic transitions of iron oxides, the near infrared atmospheric features used for atmospheric correction, and shortwave infrared mineral absorption features. Applying this model to EMIT's radiometric reference observation, we find SNR outperforms requirements by a factor of two.

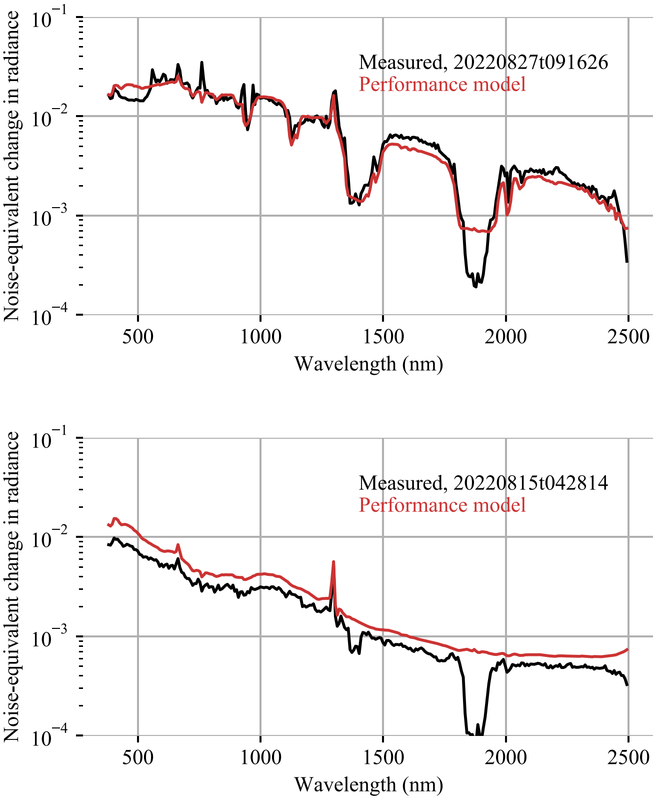

Fig. 22. Top: Modeled and measured noise levels for a bright scene. Bottom: Modeled and measured noise levels for a dark scene.

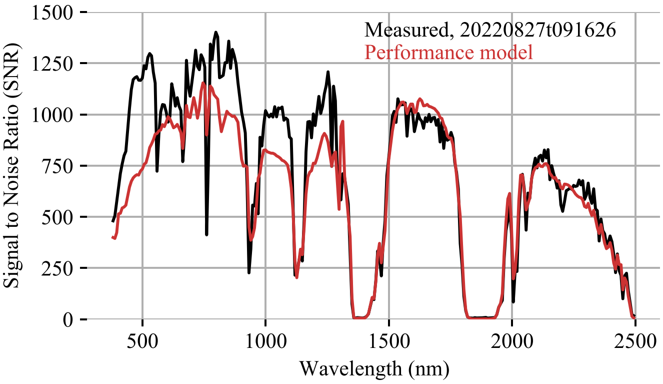

Fig. 23. SNR at the Libya 4 site.

4. Discussion

We have completed the first on-orbit characterization of the EMIT imaging spectrometer. EMIT is designed to detect small changes in mineral spectral feature depths; a change of a few percent in the depth of the hematite absorption feature, extrapolated globally, is enough to flip the sign of mineral dust radiative forcing (Li et al., 2021). EMIT's performance aims for statistical confidence in detecting such small changes. On-orbit, we find that performance surpasses these requirements (Table 1). SNR exceeds 500 for bright arid targets. An average reflectance agreement of 1% with coincident in situ data in a controlled environment approaches the fidelity of field spectroscopy (Thome, 2016). Our revised noise predictions match measurements to approximately 10% across diverse scene types. Wavelength calibrations are characterized with precision of a small fraction of 1% of a channel. These results demonstrate that EMIT is capable of high accuracy mineral mapping to achieve its science objectives.

Notably, EMIT achieves this accuracy with no shutter and no onboard calibration systems of any kind. Its design philosophy emphasizes vicarious calibration enabled by a simple optomechanical layout with high uniformity and stability. Accordingly, our on-orbit validation process makes extensive use of opportunistic targets in the Earth's surface and atmosphere. Among all optical instruments, imaging spectrometers in particular stand to benefit from this strategy. High-SNR spectrometers are highly sensitive to the inevitable errors in radiative transfer modeling, such as uncertainties in solar irradiance, atmospheric gases, or the spectral responses that sample them. By using the same radiative transfer models in calibration as the operational reflectance products, many of these errors cancel each other, enabling reflectance accuracies closer to the true SNR of the instrument. Realizing the full benefits of this strategy requires strong alignment between the methods for instrument calibration and those used for the operational surface reflectance retrieval. Historically, these steps have been considered independent and sequential, and often implemented by different teams. The EMIT experience demonstrates the value of a combined treatment in which calibration and atmospheric correction are tackled in concert with identical atmospheric modeling assumptions.

Calibration is a process rather than a result. We will continue to track radiometric accuracy and performance over time as the mission progresses. We will use bright cloud features, the reflectance of which is well-constrained in visible wavelengths, to monitor the calibration in short wavelengths. Repeat overflights of arid regions, in particular psuedo-invariant calibration sites, can also indicate changes in relative radiometry. Cross-calibration with other on-orbit instruments can assess the absolute accuracy of these calibrations and the sensitivities to downstream products. Atmospheric fits can confirm the wavelength calibration does not change over time with inevitable instrument thermal cycles. This ensures that EMIT's mineral identification products are consistent over its lifespan.

EMIT has achieved several firsts for an instrument of its class. It has demonstrated the first on-orbit FPA alignment. Our procedure measured and then removed a micron-scale FPA rotation. This is important for mapping mineral band positions, where such nonuniformities could change geologic interpretations. The same technique could also benefit future spectrometers, such as SBG, with similarly stringent measurement needs. EMIT has also improved spectral fidelity over previous grating-based instruments, with a new grating design that mitigates spectral and spatial scatter. This carries benefits for both accurate atmospheric correction and mineralogy, both of which rely on sharp high contrast absorption features. Laboratory and flight data suggest that, outside the uncalibrated order sorting filter seams, optical artifacts are at least three orders of magnitude below the primary signal. This underscores EMIT's potential for future science investigations beyond mineralogy. EMIT's on-orbit performance provides reason for optimism as we enter a new era of spectroscopic remote sensing of Earth's surface and atmosphere, for which this latest generation of sensors is only the vanguard.

CRediT authorship contribution statement

David R. Thompson: Conceptualization, Formal analysis, Investigation, Methodology, Software, Validation, Writing – original draft, Writing – review & editing. **Robert O. Green:** Conceptualization, Investigation, Methodology, Project administration, Resources, Supervision. **Christine Bradley:** Formal analysis, Investigation, Methodology. **Philip G. Brodrick:** Data curation, Investigation, Methodology, Writing – original draft, Writing – review & editing. **Natalie Mahowald:** Conceptualization, Funding acquisition, Project administration, Supervision, Writing – original draft. **Eyal Ben Dor:** Conceptualization, Investigation, Methodology. **Matthew Bennett:** Formal analysis, Investigation, Methodology, Supervision. **Michael Bernas:** Formal analysis, Investigation. **Nimrod Carmon:** Formal analysis, Investigation, Methodology, Software. **K. Dana Chadwick:** Investigation, Methodology, Supervision, Writing – original draft. **Roger N. Clark:** Conceptualization, Investigation, Methodology, Validation. **Red Willow Coleman:** Formal analysis, Investigation, Software, Validation. **Evan Cox:** Data curation, Investigation, Methodology, Writing – original draft. **Ernesto Diaz:** Investigation, Supervision. **Michael L. Eastwood:** Conceptualization, Formal analysis, Investigation, Methodology, Project administration, Writing – original draft. **Regina Eckert:** Formal analysis, Investigation, Methodology, Software, Writing – original draft. **Bethany L. Ehlmann:** Conceptualization, Investigation, Methodology, Supervision, Writing – original draft. **Paul Ginoux:** Conceptualization, Investigation, Validation. **María Gonçalves Ageitos:** Investigation, Writing – original draft. **Kathleen Grant:** Formal analysis, Investigation, Software. **Luis Guanter:** Conceptualization, Methodology, Writing – original draft. **Daniela Heller Pearlshtien:** Data curation, Investigation, Validation, Writing – original draft. **Mark Helmlinger:** Data curation, Formal analysis, Investigation, Methodology. **Harrison Herzog:** Formal analysis, Investigation. **Todd Hoefen:** Data curation, Investigation, Methodology, Validation. **Yue Huang:** Investigation, Methodology. **Abigail Keebler:** Data curation, Formal analysis, Investigation, Methodology, Validation. **Olga Kalashnikova:** Conceptualization, Methodology. **Didier Keymeulen:** Investigation, Methodology, Writing – original draft. **Raymond Kokaly:** Formal analysis, Investigation, Methodology, Validation, Writing – original draft. **Martina Klose:** Investigation, Validation, Writing – original draft. **Longlei Li:** Investigation, Validation. **Sarah R. Lundeen:** Investigation, Software, Supervision. **John Meyer:** Data curation, Investigation, Validation. **Elizabeth Middleton:** Conceptualization, Methodology. **Ron L. Miller:** Conceptualization, Methodology, Validation. **Pantazis Mouroulis:** Conceptualization, Formal analysis, Investigation, Methodology, Supervision. **Bogdan Oaida:** Formal analysis, Investigation. **Vincenzo Obiso:** Investigation, Validation, Writing – original draft. **Francisco Ochoa:** Data curation, Investigation, Methodology, Software, Validation. **Winston Olson-Duvall:** Investigation, Software. **Gregory S. Okin:** Conceptualization, Formal analysis, Investigation, Methodology, Validation. **Thomas H. Painter:** Conceptualization, Investigation, Resources. **Carlos Pérez García-Pando:** Conceptualization, Investigation, Methodology, Writing – original draft. **Randy Pollock:** Conceptualization, Investigation, Project administration. **Vincent Realmuto:** Conceptualization, Investigation, Methodology. **Lucas Shaw:** Formal analysis, Investigation. **Peter Sullivan:** Formal analysis, Investigation. **Gregg Swayze:** Conceptualization, Data curation, Investigation, Methodology, Validation. **Erik Thingvold:** Formal analysis, Investigation. **Andrew K. Thorpe:** Investigation, Methodology, Writing – original draft. **Suresh Vannan:** Supervision. **Catalina Villarreal:** Project administration. **Charlene Ung:** Supervision, Writing – original draft. **Daniel W. Wilson:** Formal analysis, Investigation. **Sander Zandbergen:** Formal analysis, Investigation.

Declaration of competing interest

The authors declare that they have no known competing financial interests or personal relationships that could have appeared to influence the work reported in this paper.

Data availability

The EMIT science data system code, including the level 1b radiance calibration and associated calibration files, can be found at https://github.com/emit-sds/. Spectral libraries used in the surface/atm fits are downloadable from the ECOSIS library at https://ecosis.org/package/emit-manually-adjusted-snow-and-liquids-reflectance-spectra, https://ecosis.org/package/emit-manually-adjusted-vegetation-reflectance-spectra, and https://ecosis.org/package/emit-manually-adjusted-water-reflectance-spectra.

Acknowledgment

EMIT is supported by the National Aeronautics and Space Administration Earth Venture Instrument program, under the Earth Science Division of the Science Mission Directorate. K. Dana Chadwick is supported by the NASA Applied Sciences Program. Carlos Pérez García-Pando and María Gonçalves Ageitos acknowledge support from the European Research Council (ERC) Consolidator Grant FRAGMENT (grant agreement No. 773051), and the AXA Chair on Sand and Dust Storms at the Barcelona Supercomputing Center funded by the AXA Research Fund. Martina Klose has received funding through the Helmholtz Association's Initiative and Networking Fund (grant agreement No. VH-NG-1533). We thank Jeffrey Czapla-Myers and the University of Arizona team for their maintenance and operation of the Railroad Valley automated calibration facility. This research was performed at the Jet Propulsion Laboratory, California Institute of Technology, under a contract with the National Aeronautics and Space Administration. We acknowledge the support and assistance of NASA's International Space Station Program. The USGS authors' contribution to this published Work was prepared by U.S. federal government employees as part of their official duties and constitutes a "work of the United States government," and is considered to be in the public domain and therefore domestic copyright does not apply. Any use of trade, firm, or product names is for descriptive purposes only and does not imply endorsement by the U.S. Government. Copyright 2024 California Institute of Technology. All rights reserved. US Government Support Acknowledged.

References

Alonso, K., Bachmann, M., Burch, K., Carmona, E., Cerra, D., De los Reyes, R., Dietrich, D., Heiden, U., Hölderlin, A., Ickes, J., et al., 2019. Data products, quality and validation of the dlr earth sensing imaging spectrometer (desis). Sensors 19, 4471.

Asner, G.P., Knapp, D.E., Boardman, J., Green, R.O., Kennedy-Bowdoin, T., Eastwood, M., Martin, R.E., Anderson, C., Field, C.B., 2012. Carnegie airborne observatory-2: increasing science data dimensionality via high-fidelity multi-sensor fusion. Remote Sens. Environ. 124, 454–465.

Berk, A., Conforti, P., Kennett, R., Perkins, T., Hawes, F., van den Bosch, J., 2014. MODTRAN® 6: A major upgrade of the MODTRAN® radiative transfer code. In: IEEE Hyperspectral Image and Signal Processing: Evolution in Remote Sensing (WHISPERS), 2014 6th Workshop on, pp. 1–4.

Boardman, J.W., Kruse, F.A., 2011. Analysis of imaging spectrometer data using *n*-dimensional geometry and a mixture-tuned matched filtering approach. IEEE Trans. Geosci. Remote Sens. 49, 4138–4152.

Bouvet, M., Thome, K., Berthelot, B., Bialek, A., Czapla-Myers, J., Fox, N.P., Goryl, P., Henry, P., Ma, L., Marcq, S., et al., 2019. Radcalnet: A radiometric calibration network for earth observing imagers operating in the visible to shortwave infrared spectral range. Remote Sens. 11, 2401.

Bradley, C.L., Thingvold, E., Moore, L.B., Haag, J.M., Raouf, N.A., Mouroulis, P., Green, R.O., 2020. Optical design of the earth surface mineral dust source investigation (emit) imaging spectrometer. In: Imaging Spectrometry XXIV: Applications, Sensors, and Processing, volume 11504. SPIE, p. 1150402.

Brodrick, P., Green, R.O., Thompson, D.R., Mahowald, N.M., Clark, R.N., Swayze, G.A., Kokaly, R.F., Meyer, J.M., Ochoa, F., Okin, G.S., Grant, K., Ehlmann, B.L., Keebler, A., Coleman, R.W.W., Cox, E., Ginoux, P.A., Hoefen, T.M., Kalashnikova, O. V., Miller, R.L., Painter, T., Perez, C., García-Pando, C.P., Realmuto, V.J., Ben-dor, E., Lundeen, S., Olson-Duvall, W., Li, L., Pearlshtien, D.H., Obiso, V., Gonçalves, M., Zastko, L., Phillips, B.R., Reath, K., Vannan, S., Ung, C., 2023. The Earth Surface Mineral Dust Source Investigation (Emit): Global Distributions of Minerology in Arid Lands. American Geophysical Union Fall Meeting. GC53B-05.

Bruegge, C.J., Arnold, G.T., Czapla-Myers, J., Dominguez, R., Helmlinger, M.C., Thompson, D.R., Van den Bosch, J., Wenny, B.N., 2021. Vicarious calibration of Emas, airmspi, and aviris sensors during firex-aq. IEEE Trans. Geosci. Remote Sens. 59, 10286–10297.

Carmon, N., Thompson, D.R., Bohn, N., Susiluoto, J., Turmon, M., Brodrick, P.G., Connelly, D.S., Braverman, A., Cawse-Nicholson, K., Green, R.O., Gunson, M., 2020. Uncertainty quantification for a global imaging spectroscopy surface composition investigation. Remote Sens. Environ. 251, 112038.

Cawse-Nicholson, K., Townsend, P.A., Schimel, D., Assiri, A.M., Blake, P.L., Buongiorno, M.F., Campbell, P., Carmon, N., Casey, K.A., Correa-Pabón, R.E., et al., 2021. Nasa's surface biology and geology designated observable: A perspective on surface imaging algorithms. Remote Sens. Environ. 257, 112349.

Chabrillat, S., Guanter, L., Segl, K., Foerster, S., Fischer, S., Rossner, G., Schickling, A., LaPorta, L., Honold, H.-P., Storch, T., 2020. The enmap german spaceborne imaging spectroscopy mission: Update and highlights of recent preparatory activities. In: IGARSS 2020–2020 IEEE International Geoscience and Remote Sensing Symposium. IEEE, pp. 3278–3281.

Chapman, J., Thompson, D.R., Helmlinger, M.C., Eastwood, M.L., Bue, B.D., Geier, S., Green, R.O., Lundeen, S.R., Olson-Duvall, W., 2019. Spectral and radiometric calibration of the next generation airborne visible infrared spectrometer (AVIRIS-NG). Remote Sens. 11.

Cogliati, S., Sarti, F., Chiarantini, L., Cosi, M., Lorusso, R., Lopinto, E., Miglietta, F., Genesio, L., Guanter, L., Damm, A., et al., 2021. The prisma imaging spectroscopy mission: overview and first performance analysis. Remote Sens. Environ. 262, 112499.

Connelly, D.S., Thompson, D.R., Mahowald, N.M., Li, L., Carmon, N., Okin, G.S., Green, R.O., 2021. The emit mission information yield for mineral dust radiative forcing. Remote Sens. Environ. 258, 112380.

Cook, G., 2004. Capabilities and accommodations on the iss express pallet. In: 42nd AIAA Aerospace Sciences Meeting and Exhibit, p. 439.

Dennison, P.E., Gardner, M.E., 2000. Hawaii 2000 vegetation species spectra. In: Data set. https://doi.org/10.21232/C2HT0K. Available on-line [http://ecosis.org] from the Ecological Spectral Information System (EcoSIS).

Fischler, M.A., Bolles, R.C., 1981. Random sample consensus: a paradigm for model fitting with applications to image analysis and automated cartography. Commun. ACM 24, 381–395.

Fontenla, J., Harder, J., Livingston, W., Snow, M., Woods, T., 2011. High-resolution solar spectral irradiance from extreme ultraviolet to far infrared. J. Geophys. Res. Atmos. 116.

Goetz, A.F., Srivastava, V., 1985. Mineralogical mapping in the cuprite mining district, nevada. In: Proceedings of the Airborne Imaging Spectrometer (AIRS) Data Analysis Workshop: Jet Propulsion Laboratory Publication, 85-41, 22–29.

Green, R., Pieters, C., Mouroulis, P., Eastwood, M., Boardman, J., Glavich, T., Isaacson, P., Annadurai, M., Besse, S., Barr, D., et al., 2011. The moon mineralogy mapper (M3) imaging spectrometer for lunar science: instrument description, calibration, on-orbit measurements, science data calibration and on-orbit validation. J. Geophys. Res. Planets 116.

Green, R.O., Mahowald, N., Ung, C., Thompson, D.R., Bator, L., Bennet, M., Bernas, M., Blackway, N., Bradley, C., Cha, J., et al., 2020. The earth surface mineral dust source investigation: An earth science imaging spectroscopy mission. In: In 2020 IEEE Aerospace Conference. IEEE, pp. 1–15.

Green, R.O., et al., 2022. EMIT Mission Data Products. Data available from https://lpdaac.usgs.gov/,.

Guanter, L., Estellés, V., Moreno, J., 2007. Spectral calibration and atmospheric correction of ultra-fine spectral and spatial resolution remote sensing data. Application to casi-1500 data. Remote Sens. Environ. 109, 54–65.

Guanter, L., Kaufmann, H., Segl, K., Foerster, S., Rogass, C., Chabrillat, S., Kuester, T., Hollstein, A., Rossner, G., Chlebek, C., et al., 2015. The enmap spaceborne imaging spectroscopy mission for earth observation. Remote Sens. 7, 8830–8857.

Helmlinger, M., Eastwood, M., Green, R., Thompson, D.R., 2016. Solar-similar near-infrared suppressed "blue" calibration source. In: In 2016 IEEE Aerospace Conference. IEEE, pp. 1–11.

Herold, M., Roberts, D.A., Gardner, M.E., Dennison, P.E., 2004. Spectrometry for urban area remote sensing—development and analysis of a spectral library from 350 to 2400 nm. Remote Sens. Environ. 91, 304–319. Data set available on-line [http://ecosis.org] from the Ecological Spectral Information System (EcoSIS).

Keymeulen, D., Pham, T., Klimesh, M., Allen, G., Flesch, G., Valencia, R., Xie, H., Kiely, A., Dolman, D., Roth, K., Crocker, K., Whitlock, T., Holyoake, C., Burchfiel, S., Kampf, F., Kentley, M., Robson, A., Schepps, A., Lazaravich, B., Stocek, D., 2022. Data compression and cloud screening using a high-performance embedded system-on-a-chip for the earth surface mineral dust source investigation (emit) imaging spectrometer on the international space station (iss). In: In 8th INTERNATIONAL WORKSHOP ON ON-BOARD PAYLOAD DATA COMPRESSION (OBPDC 2022). ESA, CNES.

Kokaly, R., Clark, R., Swayze, G., Livo, K., Hoefen, T., Pearson, N., Wise, R., Benzel, W., Lowers, H., Driscoll, R., Klein, A., 2017. USGS Spectral Library Version 7. U.S. Geological Survey Data, Series 1031, p. 61.

Kruse, F.A., Lefkoff, A., Boardman, J., Heidebrecht, K., Shapiro, A., Barloon, P., Goetz, A., 1993. The spectral image processing system (sips)—interactive visualization and analysis of imaging spectrometer data. Remote Sens. Environ. 44, 145–163.

Li, L., Mahowald, N.M., Miller, R.L., Pérez García-Pando, C., Klose, M., Hamilton, D.S., Gonçalves Ageitos, M., Ginoux, P., Balkanski, Y., Green, R.O., et al., 2021. Quantifying the range of the dust direct radiative effect due to source mineralogy uncertainty. Atmos. Chem. Phys. 21, 3973–4005.

Matsunaga, T., Iwasaki, A., Tachikawa, T., Tanii, J., Kashimura, O., Mouri, K., Inada, H., Tsuchida, S., Nakamura, R., Yamamoto, H., et al., 2020. Hyperspectral imager suite (hisui): Its launch and current status. In: IGARSS 2020–2020 IEEE International Geoscience and Remote Sensing Symposium. IEEE, pp. 3272–3273.

Meyer, J., Kokaly, R.F., Hoefen, T., Cox, E., 2023a. Reflectance Spectra Collected August 21, at Black Rock Desert, nevada, with an ASD© FieldSpec® 4 Hi-Res NG Spectrometer for Calibration/Validation of Imaging Spectrometer Data. U.S. Geological Survey data release. https://doi.org/10.5066/P94QAHLC.

Meyer, J., Kokaly, R.F., Hoefen, T., Cox, E., Swayze, G., 2023b. Reflectance Spectra Collected August 16, at Smith Creek Playa, nevada, with an ASD© FieldSpec® 4 Hi-Res NG Spectrometer for Calibration/Validation of Imaging Spectrometer Data. U.S. Geological Survey data release. https://doi.org/10.5066/P9E2TSDF.

Mishra, N., Helder, D., Angal, A., Choi, J., Xiong, X., 2014. Absolute calibration of optical satellite sensors using Libya 4 pseudo invariant calibration site. Remote Sens. 6, 1327–1346.

Mouroulis, P., Wilson, D.W., Maker, P.D., Muller, R.E., 1998. Convex grating types for concentric imaging spectrometers. Appl. Opt. 37, 7200–7208.

Nieke, J., Rast, M., 2018. Towards the copernicus hyperspectral imaging mission for the environment (chime). In: Igarss 2018–2018 Ieee International Geoscience and Remote Sensing Symposium. IEEE, pp. 157–159.

Olson-Duvall, W., Brodrick, P., Lundeen, S., Smyth, M., Thompson, D.R., 2022. Earth Mineral dust source InvesTigation Science Data System. Open Source codebase at https://github.com/emit-sds.

Richardson, M.T., Thompson, D.R., Kurowski, M.J., Lebsock, M.D., 2021. Boundary layer water vapour statistics from high-spatial-resolution spaceborne imaging spectroscopy. Atmos. Meas. Tech. 14, 5555–5576.

Schläpfer, D., Borel, C.C., Keller, J., Itten, K.I., 1998. Atmospheric precorrected differential absorption technique to retrieve columnar water vapor. Remote Sens. Environ. 65, 353–366.

Sullivan, P., Bernas, M., Liggett, E., Eastwood, M., Green, R., 2017. Characterization of the teledyne chroma hgcdte detector for imaging spectrometers. In: In 2017 IEEE Aerospace Conference. IEEE, pp. 1–7.

Thome, K., 2016. Calibration/validation error budgets, uncertainties, traceability and their importance to imaging spectrometry. In: In 2016 IEEE International Geoscience and Remote Sensing Symposium (IGARSS). IEEE, pp. 1912–1915.

Thompson, D.R., Gao, B.-C., Green, R.O., Roberts, D.A., Dennison, P.E., Lundeen, S.R., 2015. Atmospheric correction for global mapping spectroscopy: Atrem advances for the hyspiri preparatory campaign. Remote Sens. Environ. 167, 64–77.

Thompson, D.R., Boardman, J.W., Eastwood, M.L., Green, R.O., Haag, J.M., Mouroulis, P., Gorp, B.V., 2018a. Imaging spectrometer stray spectral response: in-flight characterization, correction, and validation. Remote Sens. Environ. 204, 850–860.

Thompson, D.R., Natraj, V., Green, R.O., Helmlinger, M., Gao, B.-C., Eastwood, M., 2018b. Optimal estimation for imaging spectrometer atmospheric correction. Remote Sens. Environ. 216, 355–373.

Thompson, D.R., Cawse-Nicholson, K., Erickson, Z., Fichot, C.G., Frankenberg, C., Gao, B.-C., Gierach, M.M., Green, R.O., Jensen, D., Natraj, V., Thompson, A., 2019a. A unified approach to estimate land and water reflectances with uncertainties for coastal imaging spectroscopy. Remote Sens. Environ. 231, 111198.

Thompson, D.R., Duvall, W.O., Brodrick, P., et al., 2019b. ISOFIT: Imaging Spectrometer Optimal FITting. Open Source codebase with examples at https://github.com/isofit/isofit,.

Thompson, D.R., Brodrick, P.G., Cawse-Nicholson, K., Dana Chadwick, K., Green, R.O., Poulter, B., Serbin, S., Shiklomanov, A.N., Townsend, P.A., Turpie, K.R., 2021. Spectral fidelity of earth's terrestrial and aquatic ecosystems. Journal of Geophysical Research: Biogeosciences 126, e2021JG006273.

Thorpe, A.K., Green, R.O., Thompson, D.R., Brodrick, P.G., Chapman, J.W., Elder, C.D., Irakulis-Loitxate, I., Cusworth, D.H., Ayasse, A.K., Duren, R.M., Frankenberg, C., Guanter, L., Worden, J.R., Dennison, P.E., Roberts, D.A., Chadwick, K.D., Eastwood, M.L., Fahlen, J.E., Miller, C.E., 2023. Attribution of individual methane and carbon dioxide emission sources using emit observations from space. Sci. Adv. 9, eadh2391.

Vermote, E., El Saleous, N., Justice, C., Kaufman, Y., Privette, J., Remer, L., Roger, J., Tanre, D., 1997. Atmospheric correction of visible to middle-infrared eos-modis data over land surfaces: background, operational algorithm and validation. J. Geophys. Res. Atmos. 102, 17131–17141.

Wagner, E.P., Merz, J., Townsend, P.A., 2018. Ecological spectral information system: an open spectral library. In: AGU Fall Meeting Abstracts (pp. B41L–2878). Volume 2018.

Zandbergen, S.R., Mouroulis, P., Small, Z., Bender, H.A., Bellardo, J., 2020. Snow and water imaging spectrometer: final instrument characterization. In: Imaging Spectrometry XXIV: Applications, Sensors, and Processing, pp. 27–39. SPIE volume 11504.

Zong, Y., Brown, S.W., Johnson, B.C., Lykke, K.R., Ohno, Y., 2006. Simple spectral stray light correction method for array spectroradiometers. Appl. Opt. 45, 1111–1119.